

# The Chilean Tornado Outbreak of May 2019

## Synoptic, Mesoscale, and Historical Contexts

José Vicencio, Roberto Rondanelli, Diego Campos, Raúl Valenzuela,  
René Garreaud, Alejandra Reyes, Rodrigo Padilla, Ricardo Abarca,  
Camilo Barahona, Rodrigo Delgado, and Gabriela Nicora

**ABSTRACT:** In late May 2019, at least seven tornadoes were reported within a 24-h period in southern Chile (western South America, 36°–38°S), including EF1 and EF2 events causing substantial damage to infrastructure, dozens of injuries, and one fatality. Despite anecdotal evidence and chronicles of similar historical events, the threat from tornadoes in Chile was regarded with skepticism until the 2019 outbreak. Herein, we describe the synoptic-scale features instrumental in the development of these tornadic storms, including an extended southwest–northeast trough along the South Pacific, with a large postfrontal instability area. Tornadic storms appear to be embedded in a modestly unstable environment (positive convective available potential energy but less than 1,000 J kg<sup>-1</sup>) and strong low- and midlevel wind shear, with high near-surface storm-relative helicity values (close to  $-200 \text{ m}^2 \text{ s}^{-2}$ ), clearly differing from the Great Plains tornadoes in North America (with highly unstable environments) but resembling cold-season tornadoes previously observed in the midlatitudes of North America, Australia, and Europe. Reanalyzing rainfall and lightning data from the last 10 years, we found that tornadic storms in our region occur associated with locally extreme values of both CAPE and low-level wind shear, where a combination of the two in a low-level vorticity generation parameter appears as a simple first-order discriminant between tornadic and nontornadic environments. Future research should thoroughly examine historical events worldwide to assemble a database of high-shear, low-CAPE midlatitude storms and help improve our understanding of these storms' underlying physics.

**KEYWORDS:** South America; Mesoscale systems; Convective clouds; Extreme events; Tornadoes

<https://doi.org/10.1175/BAMS-D-19-0218.1>

Corresponding author: Roberto Rondanelli, [ronda@dgf.uchile.cl](mailto:ronda@dgf.uchile.cl)

Supplemental material: <https://doi.org/10.1175/BAMS-D-19-0218.2>

In final form 25 November 2020

©2021 American Meteorological Society

For information regarding reuse of this content and general copyright information, consult the [AMS Copyright Policy](#).

**AFFILIATIONS:** **Vicencio and Campos**—Dirección Meteorológica de Chile, and Departamento de Geofísica, Universidad de Chile, Santiago, Chile; **Rondanelli and Garreaud**—Departamento de Geofísica, Universidad de Chile, and Center for Climate and Resilience Research, Santiago, Chile; **Valenzuela**—Center for Climate and Resilience Research, Santiago, and Instituto de Ciencias de la Ingeniería, Universidad de O'Higgins, Rancagua, Chile; **Reyes, Padilla, Abarca, Barahona, and Delgado**—Dirección Meteorológica de Chile, Santiago, Chile; **Nicora**—CEILAP, UNIDEF (MINDEF-CONICET), Buenos Aires, Argentina

On 30 and 31 May 2019, two destructive tornadoes were reported in two of southern Chile's large cities (Fig. 1). The first affected Los Ángeles (37.5°S) on 30 May, reaching an intensity of EF2 on the enhanced Fujita scale, according to the Chilean Weather Service (Vicencio et al. 2019), with estimated maximum sustained winds between 50 and 60 m s<sup>-1</sup> that caused severe damage along its 5-km trajectory. On 31 May, another tornado was reported as crossing the second-largest metropolitan area in the country along a 15-km trajectory between Talcahuano and Concepción (36.8°S), with estimated winds between 50 and 55 m s<sup>-1</sup> (EF1–EF2; Aránguiz et al. 2020; see also the appendix). During the two days, at least five other tornadoes were reported by emergency agencies, social networks, and newspapers in small towns and country areas, resulting in roof damage, displacement of vehicles, personal injuries, and one fatality (Table 1 summarizes all tornadoes and damage reports). This tornado outbreak occurred over a period of 24 h amid severe weather conditions that also included lightning, heavy rain, and large hail (~3 cm in diameter), all of which are uncommon in south-central Chile's generally more stable extratropical storms.

Tornadoes are considered to be among the most damaging weather events, causing millions of dollars' worth of damage and dozens of casualties annually (Brooks and Doswell 2001). The effects of tornadoes are widely known in regions where they are frequently reported, notably in the Great Plains of the central and southern United States. This area, colloquially known as "Tornado Alley," reports nearly 800 tornadoes annually (Goliger and Milford 1998)—the highest frequency on Earth—mostly

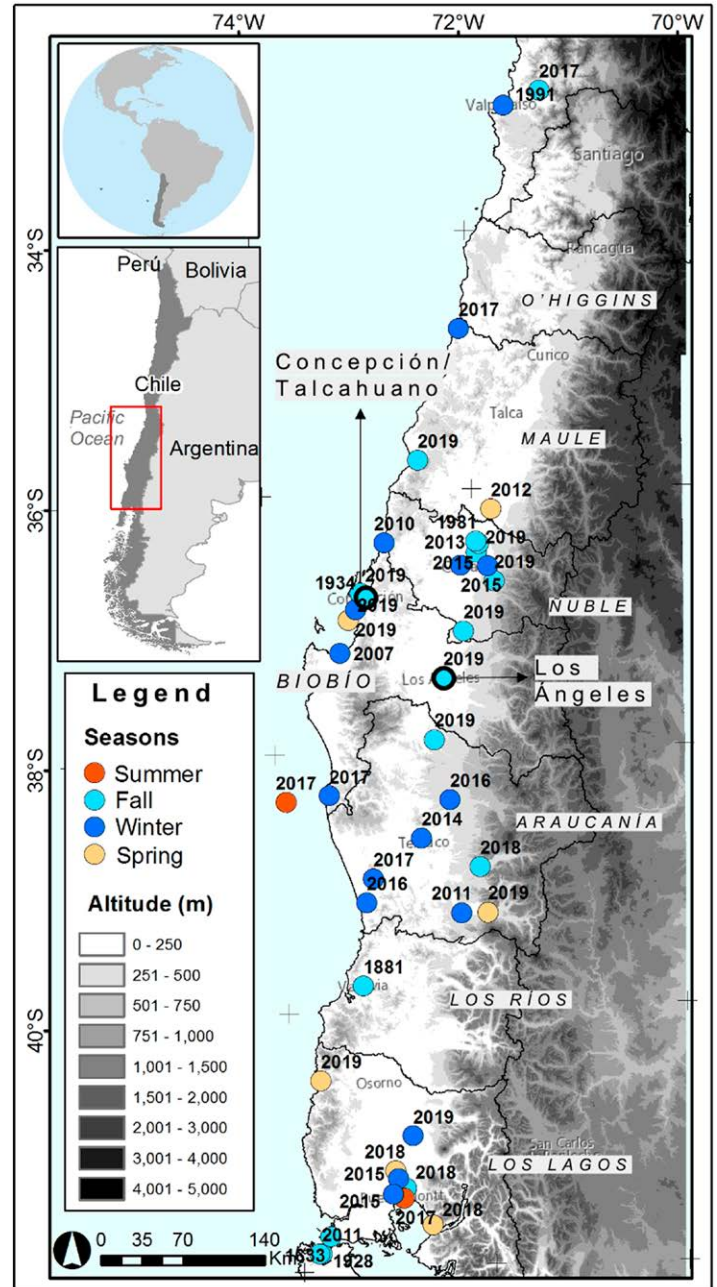


**Fig. 1.** Geographical location of central and southern Chile, including the position of 37 reported tornadoes (filled circles) from 1633 to 2019, including season (color) and year of occurrence, according to Servicio Meteorológico de la Armada (2010) and our own elaboration. The positions of Talcahuano–Concepción and Los Ángeles are shown with the black outlined circles. Topography is shown in grayscale. Administrative region names are indicated in black italic font.

**Table 1. Main features of all tornadoes reported between 30 and 31 May 2019, including informed location, hour, estimated intensity, path, and main observed damage. Report source: ONEMI (National Emergency Management Office), newspapers, DMC technical report, and social networks.**

No.	Location (city/town, region)	Lat, lon	Time and date	Duration, path distance, EF scale (estimated maximum winds)	Supercellular features (total life, storm direction and speed, IR features)	Main observed damage according to different evidence and reports
1	San Carlos/Quileto, Ñuble	36.503°S, 71.973°W	~1900 UTC 30 May		2 h 20 min, 330°, 10 m s <sup>-1</sup>	Roof damage and falling tree branches
2	San Miguel de Itata, Yungay, Biobío	37.106°S, 72.119°W	~1920 UTC 30 May		(1720–2030 UTC) 3 h 10 min, 318°, 10 m s <sup>-1</sup> , enhanced V	Roof damage, broken glass, and lamp posts destroyed 28 houses with minor damage, 14 houses with roof damage
3	Coihueco Ñuble	36.726°S, 71.810°W	~2000 UTC 30 May		2 h 20 min, 330°, 10 m s <sup>-1</sup> (same storm as tornado no. 1), enhanced V, coldest temperature updraft before tornado	Roof damage, falling tree branches, and lamp posts destroyed Complete destruction of a wooden public dining room
4	Los Ángeles, Biobío	37.463°S, 72.330°W	2157 UTC 30 May	~8 min, ~5.0 km, EF2 (60.3 m s <sup>-1</sup> )	(2000–2240 UTC) 2 h 40 min, 328°, 12 m s <sup>-1</sup> , flanking line updrafts, coldest temperature updraft before tornado	18 people injured 345 people affected 11 houses destroyed, 119 with major damage and 213 houses with minor damage 1 wooden building completely destroyed Truck and cars displaced Fallen trees Roads blocked and affected 200 people without communication services 6,769 electricity customers affected by power outages
5	Collipulli, Araucanía	37.939°S, 72.438°W	2200–2325 UTC 30 May		(2120–2310 UTC) 1 h 50 min, 328°, 12 m s <sup>-1</sup>	13 people injured 17 people affected 1 house destroyed, 1 house with major damage, and 4 other houses with minor damage
6	Talcahuano–Concepción, Biobío	36.785°S, 73.100°W	1800 UTC 31 May	15 min, 17.1 km, EF1 (42.2 m s <sup>-1</sup> )	(1540–1830 UTC) 2 h 50 min, 329°, 18 m s <sup>-1</sup> , cold U	1 person dead 23 people injured 1 house destroyed, 175 with major damage and 191 with minor damage Near 500 houses with different types of damage Around 50,000 electricity customers affected by power outages
7	Chanco, Maule	35.775°S, 72.505°W	Between 1900 and 1920 UTC 31 May		(1740–1940 UTC) 2 h, 318°, 22 m s <sup>-1</sup> , cold U	Fallen trees and power outages in rural areas Roads blocked

during boreal spring (Brooks et al. 2003). By contrast, in South America, where some of the world's most severe storms have been identified (Zipser et al. 2006), only around 7–10 tornadoes are reported per year (Goliger and Milford 1998). An area in eastern South America—south of 20°S, shared by Argentina, Brazil, Paraguay, and Uruguay—has the highest concentration of

days with favorable conditions for tornadoes, but no favorable days are shown on the western coast of South America (Brooks et al. 2003). From a sample of about 70 tornadoes registered in Brazil, no clear seasonality could be established (Silva Dias 2011).

Tornadoes in western South America and southern Chile are so rare that, prior to May 2019, the only reference in scientific literature appears to be a conference paper (Soliño and Schwarzkopf 1982) reporting the occurrence of five tornadoes between 1881 and 1981. Unconfirmed reports seem to be the origin of a slight shading over central and southern Chile appearing in a worldwide review of tornadoes, including a section about South America, mostly focused on neighboring Argentina (Goliger and Milford 1998). Because Chile lies on the southwest coast of South America, the subtropical Pacific anticyclone creates a relatively mild and stable climate, with most of its rainfall originating from cold fronts during the austral winter (Falvey and Garreaud 2007). Convection and thunderstorms are extremely infrequent in Chile compared to the rest of the continent, except in southern Patagonia (45°–50°S, Garreaud et al. 2014) and the Northern Altiplano region (Garreaud et al. 2003). Despite the relative absence of severe weather over continental Chile, reports of about 30 tornadoes and waterspouts have been collected by the Chilean Navy Weather Service since 2000 (Servicio Meteorológico de la Armada 2010). In spite of accumulated anecdotal evidence, including folklore and mythological references from pre-Columbian people (Bastias-Curivil 2019), most scientists and authorities were surprised by the tornado outbreak in late May 2019 in a country with no weather radars and no established tornado warnings. A recent independent study by Barrett et al. (2020) described the environmental and mesoscale conditions of the two main tornadoes of Los Ángeles and Talcahuano–Concepción and attributed the tornadic storms to the combination of moist warm surface air advection and cold upper-tropospheric temperatures, giving rise to convective available potential energy due to a midlevel trough. Substantial shear, potentially enhanced by the abrupt topography, was also postulated by Barrett et al. (2020) as a key contributor to tornadic storms.

However, the tornado outbreak prompted many questions, challenging our understanding of extreme meteorological events in central and southern Chile. Do Chile's environmental conditions differ from those that allow tornadoes to form in other regions of the world? What were the environmental conditions that triggered the 2019 tornado outbreak? How common are these conditions? Indeed, tornadoes in modestly buoyant environments with low convective available potential energy (CAPE) have been reported over continents' western coasts during wintertime (Braun and Monteverdi 1991; Blier and Batten 1994; Monteverdi and Quadros 1994; Hanstrum et al. 2002; Monteverdi et al. 2003) as well as other regions, such as the southeastern United States (Sherburn et al. 2016) and Europe (Clark 2009; Wesolek and Mahieu 2011). Even for high-CAPE tornadic environments, strong low-level shear (between the surface and 1–3 km) appears to be a key factor compared to the presence of convective instability (Brooks 2009; Brooks et al. 2019).

The purpose of this work is to develop a synoptic and mesoscale description of the Chilean tornadoes of 30 and 31 May 2019 as we address the abovementioned questions. We characterize the seasonality and geographical distribution of previously reported events using a tornado and waterspout database. The *GOES-16* and lightning databases and reports from the ground allowed us to describe some of the mesoscale features related to the development and evolution of convective cells during this tornado outbreak. In particular, we use Aircraft Measurement Data Relay (AMDAR) data to characterize the observed thermodynamic and shear parameters during the period of the tornado outbreak. We use the ERA5 reanalysis to investigate the role of wind shear and instability parameters in some previous tornadic storms. Besides our local interest in these tornadic storms, we expect to contribute to the larger global research effort to uncover the physical mechanisms and develop forecasting capabilities for these rare but potentially destructive tornadoes.



## Data

Here, we briefly describe the observational data and the numerical model output used in this analysis.

**GOES-16 RGB air mass.** *GOES-16* satellite data (channels 8, 10, 12, and 13) were used to make red–green–blue (RGB) air mass composites for 2100 UTC 30 May and 1800 UTC 31 May (Lensky and Rosenfeld 2008; EUMETSAT 2009, 2015). To observe the mesoscale cloud development, 10-min *GOES-16* images from channel 13 (infrared) were used.

**ERA5 and ECMWF forecast.** For synoptic analysis, we used the most unstable CAPE winds at 200, 500, 850, and 1,000 hPa; temperature at 500 and 850 hPa; geopotential height at 200, 500, 700, and 1,000 hPa; and dewpoint fields from ERA5 (~31-km horizontal resolution; Hersbach et al. 2020). Isentropic potential vorticity (PV) and wind at 330 K were also obtained from ERA-Interim reanalysis (Berrisford et al. 2009) at ~80-km horizontal resolution (Berrisford et al. 2009). In the case of sea level pressure (SLP) and 300-hPa winds, the data came from the ECMWF model ( $0.1^\circ \times 0.1^\circ$ ) initialized at 1200 UTC each day. All data were recorded from 28 to 31 May 2019 every 3 h.

**Surface data and AMDAR.** To estimate precipitation intensity and accumulated amounts, we used hourly data from 50 weather rain gauges, provided by the Chilean National Water Authority (DGA) and National Weather Service (DMC). For temperature and vertical wind structure near the tornadic storms, we used Aircraft Meteorological Data Relay (AMDAR; Painting 2003) measurements from flights that landed at and took off from Carriel Sur Airport (Talcahuano–Concepción) on 30 and 31 May 2019.

**WWLLN.** The World Wide Lightning Location Network (WWLLN, <http://wwlln.net>) currently comprises 70 sensors across all continents detecting low-frequency radio waves (sferics) emitted by lightning strokes (Virts et al. 2013; Hutchins et al. 2012). Here, we use a global database with lightning stroke localization in time and space (within ~5 km and <10- $\mu$ s accuracy; Abarca et al. 2010) from January 2008 to May 2019. The global lightning detection efficiency of WWLLN ranges between 5% and 10% (Abarca et al. 2010), although recent studies estimate this global efficiency at around 15% for the year 2017 (Koronczay et al. 2019). Because it depends significantly on the discharges' maximum current, the detection efficiency can reach up to 35% for currents exceeding ~130 kA (Abarca et al. 2010).

**WRF simulations.** A regional numerical simulation was conducted to provide atmospheric fields at a higher temporal and spatial resolution near the tornado region. The simulation was performed using the Advanced Research version of the Weather and Forecasting (WRF) Model (WRF-ARW) 4.0.3 (Skamarock et al. 2019) and ERA5 reanalysis fields as boundary and initial conditions. An outer domain, at 9-km resolution, was initialized at 0000 UTC 28 May 2019, while two-way nested domains configured at 3 and 1 km were initialized at 1200 UTC 30 May 2019 (Fig. S1 in the online supplemental material). The parameterizations used in this simulation were the Thompson microphysics scheme (Thompson et al. 2008), the Betts–Miller–Janjić cumulus parameterization (active for the outer domain only; Janjić 1994), the Rapid Radiative Transfer Model radiation parameterization (Iacono et al. 2008), the Mellor–Yamada–Nakanishi–Niino level 2.5 scheme of turbulence closure for the boundary and surface layers (Nakanishi and Niino 2004, 2006), and the Noah land surface model (Niu et al. 2011).

## Synoptic-scale environment

An important feature of the synoptic-scale environment during the tornado outbreak was the

presence of a blocking anticyclone south of 45°S (H1 in Fig. 2). This blocking anticyclone produced a split of the midlatitude jet with a reinforced subtropical branch centered at 30°S and extending poleward to about 35°S (black arrows in Fig. 2; see also Figs. 3 and 4). The blocking anticyclone effectively reversed the climatological meridional gradient of PV (Fig. 4) in the upper atmosphere over the area of 70°–90°W, which is typical of Rossby wave breaking events in this region. Cyclonic PV air is advected equatorward, while anticyclonic PV is located over the blocking high in a dipole blocking pattern (anticyclonic PV air centered at around 60°S, with cyclonic disturbances traveling at around 35°S; Figs. 3c–f). The reinforced equatorward branch of the split jet becomes a waveguide for short-wavelength baroclinic disturbances traveling from the southeast Pacific toward central and southern Chile (30°–40°S), indicated as L1, L2, L3, and L4 in the surface pressure field in Fig. 2. These lows were all embedded within a much larger-scale negatively tilted (southwest–northeast) trough that, at 0900 UTC 29 May, covered the region from about 100° to 70°W and projected well into the lower latitudes (~20°S, Fig. 3). This large-scale trough is the cyclonic side of the blocking dipole, which features a large, nearly barotropic surface response with a similarly southwest–northeast elongated surface low, reaching South America at around 0900 UTC 29 May (Fig. 5a). Over the following three days, the large-scale low moved slowly eastward

toward the continent, while the smaller-scale lows traveled along the poleward side of the subtropical jet with cloud bands rotating cyclonically around an occluded larger-scale low in a configuration that resembles a “merry-go-round” pattern (Rasmussen and Turner 2003).

At 0900 UTC 29 May 2019, the first of these disturbances can be seen as a shortwave trough with its axis at about 87°W at 35°S at 500 hPa (see Fig. 3a). As the trough moves toward the continent, it rotates cyclonically, and by 2100 UTC 30 May, the axis of the trough is mostly zonal and located near 43°S (Fig. 3d). This midlevel trough is associated with the surface low L1 (centered at about 43°S and 80°W) and with the large area of thunderstorms over the ocean between 35° and 40°S (Fig. 2a). As the midlevel circulation becomes mostly zonal, pockets of cold air at the poleward side of the subtropical jet are advected toward the continent (Figs. 5 and 6), replacing the relatively warm midtropospheric air present before 0900 UTC 30 May (Figs. 6a,b). From an upper-level dynamics perspective, these pockets of cold air may be considered cyclonic PV anomalies propagating along the poleward flank of the subtropical jet (Fig. 3) or as shortwaves in the 500-hPa geopotential height field. By 2100 UTC 30 May, the midlevel trough

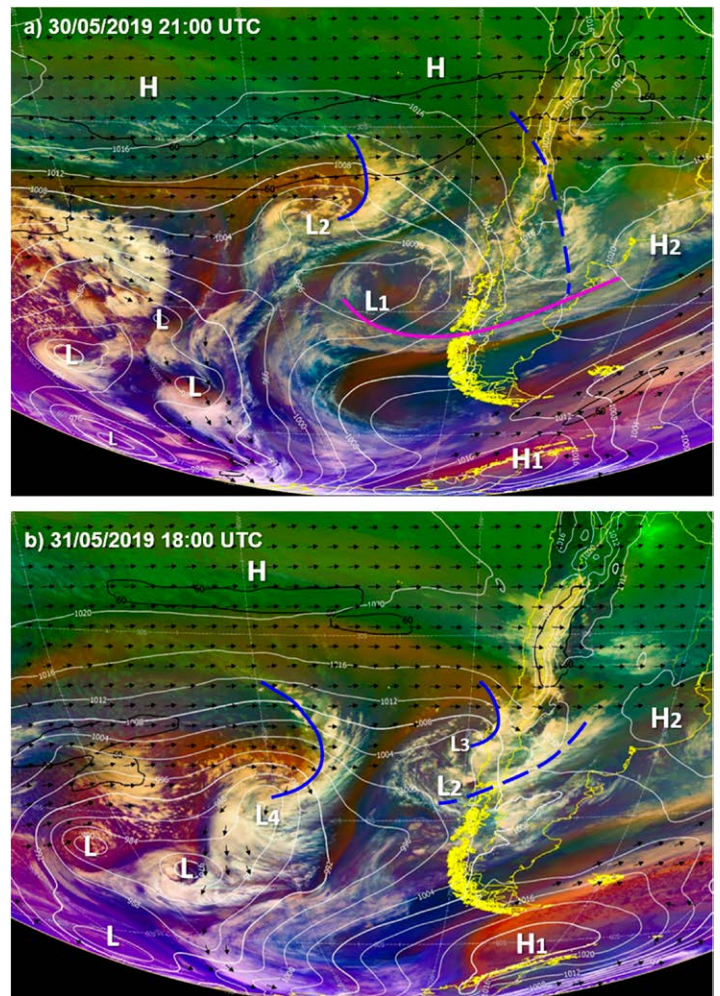


**Fig. 2.** Air mass RGB composite from *GOES-16* (colors), sea level pressure every 2 hPa (white lines), and winds at 300 hPa  $> 40 \text{ m s}^{-1}$  (black arrows) and  $> 60 \text{ m s}^{-1}$  (black contours) for (a) 2100 UTC 30 May 2019 and (b) 1800 UTC 31 May 2019. Cold and occluded front symbols (blue and magenta lines, respectively) and approximate location of high (H) and low (L) pressure centers are included. Important pressure centers are numbered (see in text). Synoptic data obtained from ECMWF ( $0.1^\circ \times 0.1^\circ$ ).



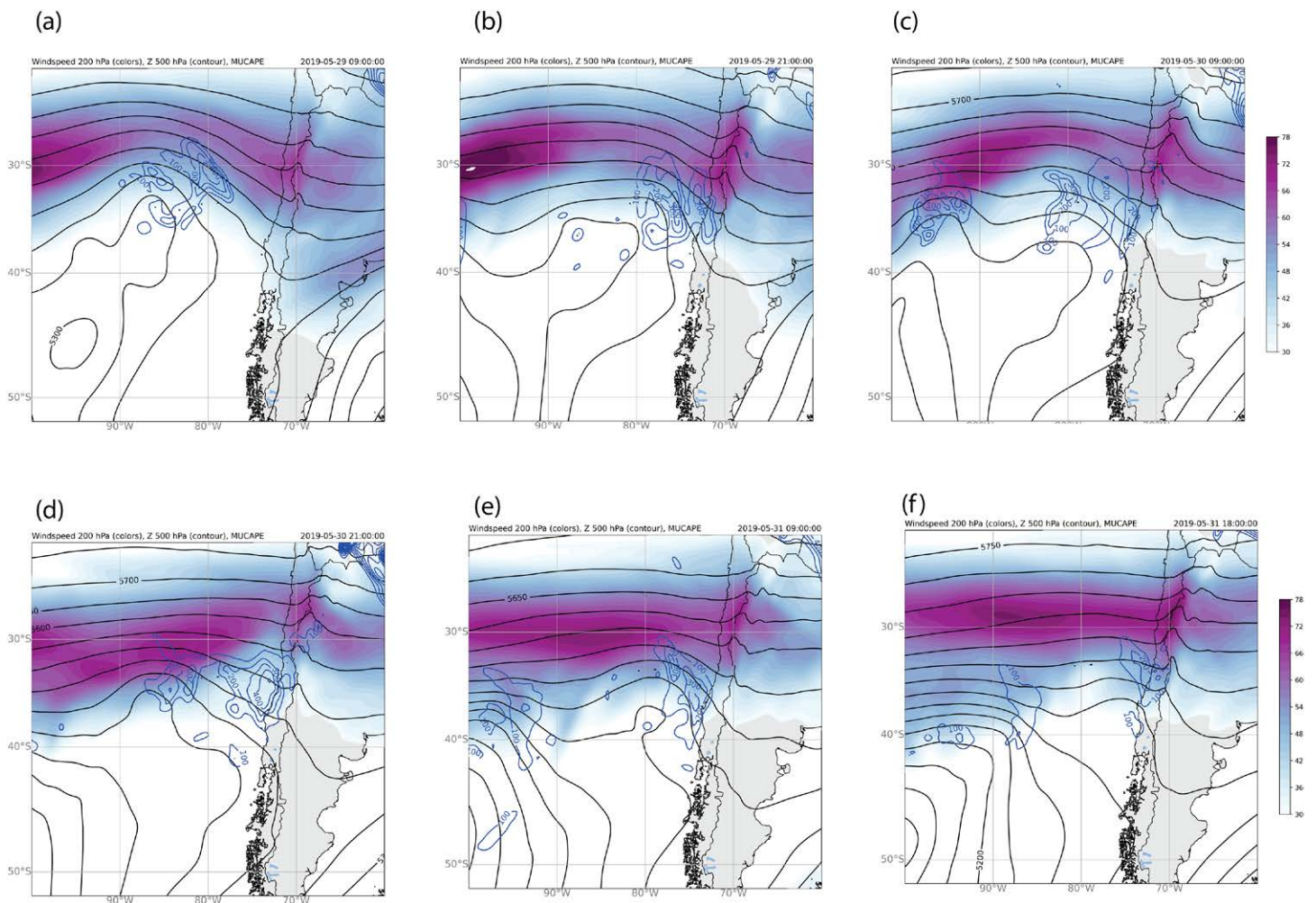


**Fig. 3.** (a)–(f) Wind at 200 hPa (colors;  $\text{m s}^{-1}$ ), geopotential height at 500 hPa (black contours; m), and the most unstable CAPE ( $\text{J kg}^{-1}$ ; red contours). Atmospheric fields are from the ERA5 reanalysis.

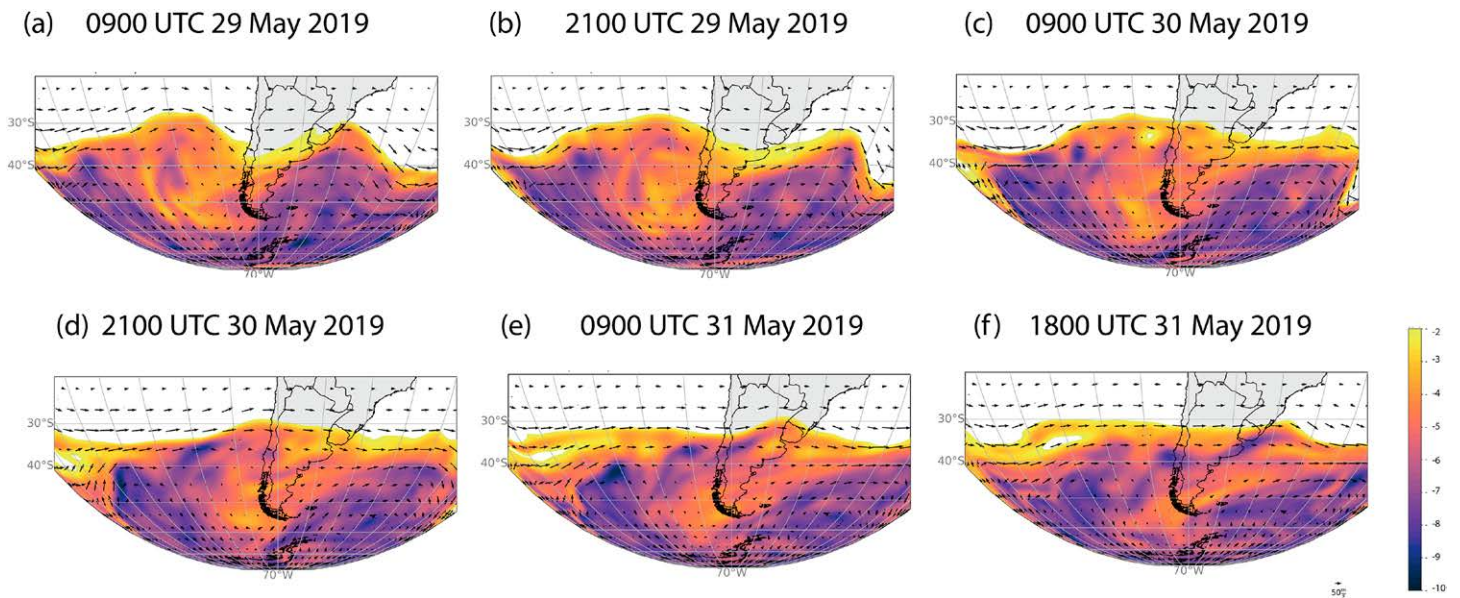


**Fig. 4.** Potential vorticity on the 330-K isentropic surface (color; PV units;  $1 \text{ PVU} = 10^{-6} \text{ K kg}^{-1} \text{ m}^2 \text{ s}^{-1}$ ) and wind on the 330-K isentropic surface. Atmospheric fields are from ERA-Interim reanalysis.



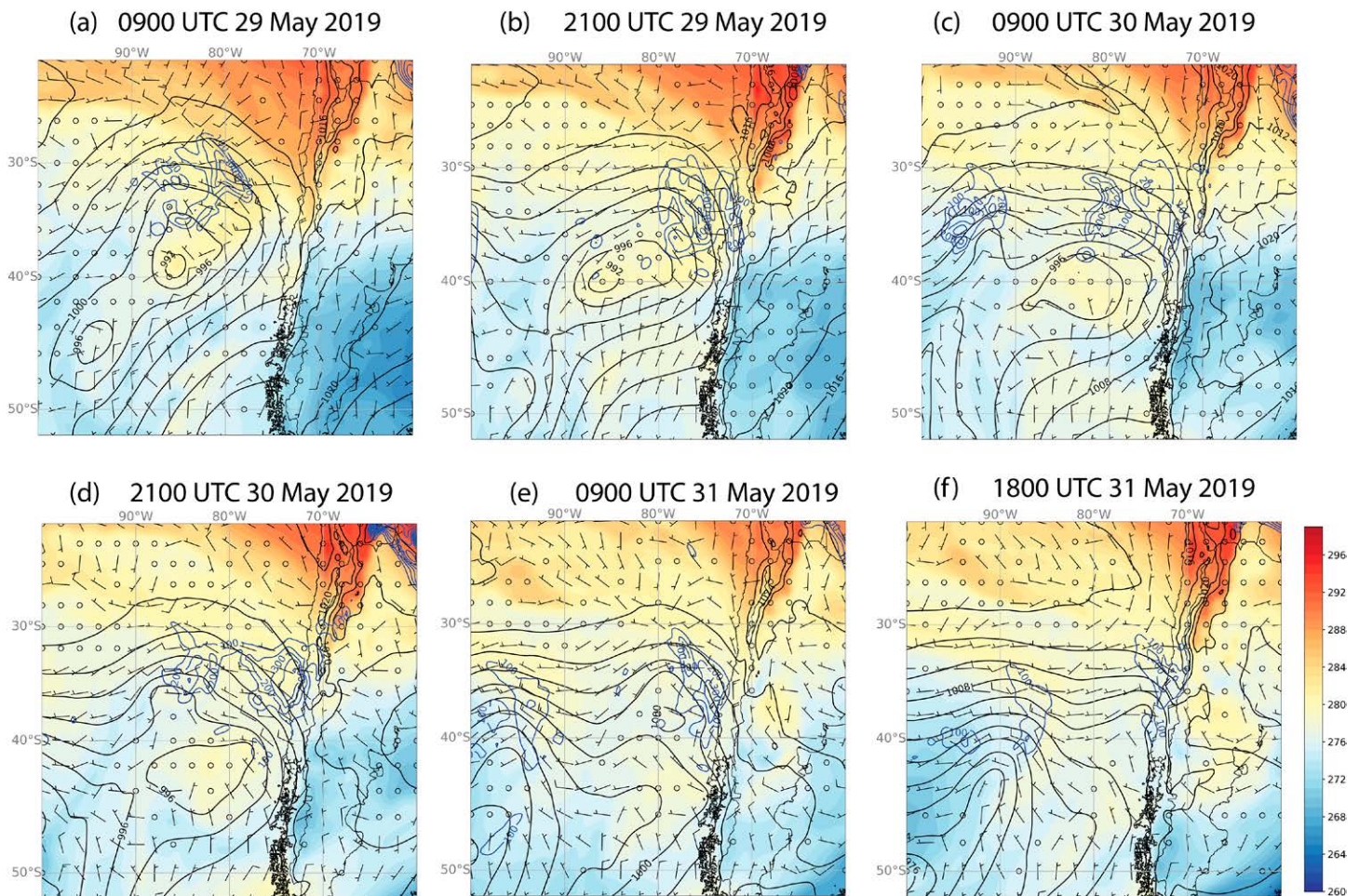


**Fig. 5.** Mean sea level pressure (hPa; black contours), wind shear between 850 hPa and the surface (barbs;  $\text{m s}^{-1}$ ), temperature at 850 hPa (K; colors), most unstable CAPE ( $\text{J kg}^{-1}$ ; blue contours) for (a) 0900 UTC 29 May 2019, (b) 2100 UTC 29 May 2019, (c) 0900 UTC 30 May 2019, (d) 2100 UTC 30 May 2019, (e) 0900 UTC 31 May 2019, and (f) 1800 UTC 31 May 2019. Atmospheric fields are from the ERA5 reanalysis.

was already located south of the tornado region with a mostly zonal orientation (Fig. 3d). The passage of the midlevel wave destabilized the troposphere, with relatively large convective instability values, as shown by the most unstable CAPE values in the ERA5 reanalysis—up to  $400\text{--}500 \text{ J kg}^{-1}$  with a peak at 2100 UTC 30 May, close to the time the first tornadoes were reported (Fig. 6d). Instability was enhanced by low-level warm advection along the coast that peaked on 30 May, induced by the surface low L1 that remained mostly stationary from about 28 to 31 May (Fig. 5). This warm advection is illustrated by the flow across isolines of geopotential thickness in the layer between 1,000 and 700 hPa (see Figs. 6a–d). Barrett et al. (2020) discuss the possible role of topography in enhancing the northerly flow along the coast, thereby favoring both low-level warm advection and helicity, particularly during the first day of the outbreak. At the same time, the main convective instability area was located in the poleward region of a jet streak exit (Fig. 3d), where synoptic-scale dynamical ascent is expected to be enhanced by secondary ageostrophic circulations (Hanstrum et al. 2002; Rose et al. 2004; Wesolek and Mahieu 2011; Childs et al. 2018), characteristic of cold-season tornado outbreaks elsewhere (Reed and Blier 1986; Monteverdi and Quadros 1994).

On 30 May, the main low L1 became occluded with a minimum pressure of about 995 hPa (Fig. 2a) and a secondary low formed on the equatorward flank of the original low (L2 in Fig. 2a, also Fig. 5d). This surface low is connected to a second midlevel shortwave trough, whose axis is at about  $85^\circ\text{W}$  at 2100 UTC 30 May (Fig. 3d). The RGB satellite image for 2100 UTC 30 May (Fig. 2a) shows a developing surface cyclone L2 with a distinct cold frontal band and a clear



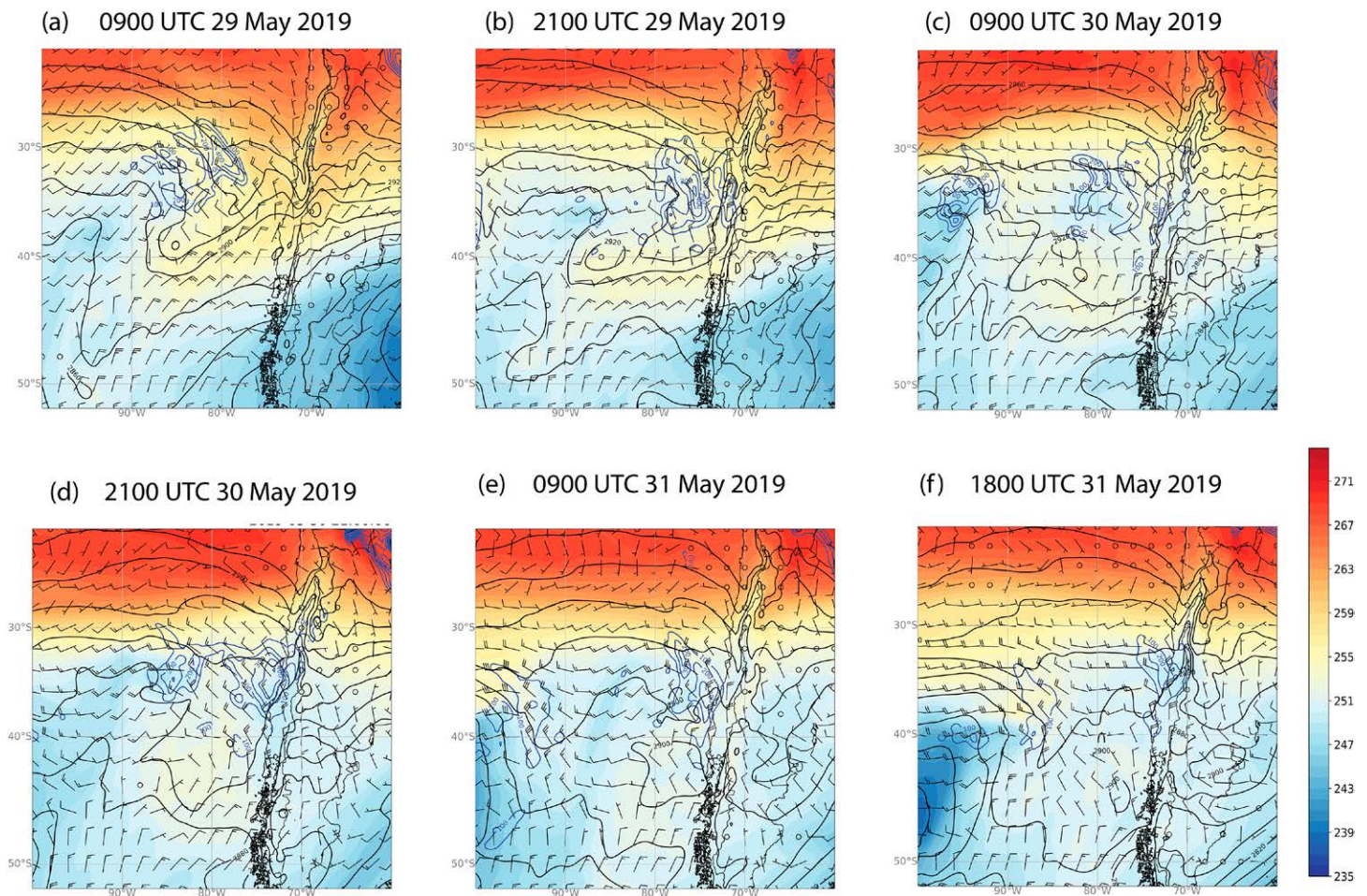


**Fig. 6.** Wind at 850 hPa (barbs;  $\text{m s}^{-1}$ ), thickness between 1,000 and 700 hPa (black contours; m), temperature at 500 hPa (color shaded; K), and most unstable CAPE (blue contours;  $\text{J kg}^{-1}$ ) for (a) 0900 UTC 29 May 2019, (b) 2100 UTC 29 May 2019, (c) 0900 UTC 30 May 2019, (d) 2100 UTC 30 May 2019, (e) 0900 UTC 31 May 2019, and (f) 1800 UTC 31 May 2019. Atmospheric fields are from the ERA5 reanalysis.

separation between the upper-level dry air intrusion behind the cold front (orange colors in Fig. 2a) and the relatively warmer air mass ahead of the surface front (dark green colors). Over the course of the following day, the secondary low L2 amplified and moved eastward as it interacted with the upper-level shortwave. The original cold frontal band of L2 rotated cyclonically over the course of 31 May, crossing Chile at about  $43^{\circ}\text{S}$  (blue segmented line in Fig. 2b). Some hours before the tornadoes on 31 May, a new mesoscale cyclone (L3 in Fig. 2b) developed below the cyclonic vorticity advection region of the upper-level shortwave (a convective band is visible from about 1300 UTC over the ocean along  $80^{\circ}\text{W}$  and from  $34^{\circ}$  to  $38^{\circ}\text{S}$ ) centered at about  $38^{\circ}\text{S}$  at 1800 UTC 31 May. This new cold frontal band comprised several individual convective cells triggered over the ocean close to the continent at about 50-km intervals (see Fig. 2b; two such cells can also be seen in Fig. 10b). This feature was responsible for the storms that produced two tornadoes on the afternoon of 31 May and closely fits the description of a comma cloud, which develops baroclinically at the expense of an upper-level short wave over an unstable postfrontal air mass (Rasmussen and Turner 2003; Houze 2014). It is remarkable that a similar comma cloud feature accompanied other cold-season tornado outbreaks, such as November 1982 in California (Hales 1985; Reed and Blier 1986) and December 2006 in England (Clark 2009).

### Mesoscale analysis

Thunderstorms over the study region that accumulated up to 180 mm of rainfall between 30 and 31 May across different stations in the region (Fig. 7a) resulted in rainfall rates higher than

10 mm h<sup>-1</sup> at some stations (Fig. 7b). Moreover, on 30 May, lightning activity (Fig. 7c) over the Biobío region highlights the presence of convective clouds developing at about 1500 until 0000 UTC, moving in straight lines from northwest to southeast (320°–330°, ~10 m s<sup>-1</sup>), most originating inland and producing large hail (about 2–3-cm diameter; see Fig. S2). Between 1900 UTC 30 May and 0000 UTC 31 May, at least five tornadoes were reported (numbers 1–5 in Table 1 and Fig. 7c) along the Central Valley between 36.5° and 38°S (see Fig. 1). On 31 May, convective cells and lightning moved from the ocean toward the continent associated with the L3 low and comma cloud system (Fig. 2b). The Talcahuano–Concepción tornado (number 6 in Table 1 and Fig. 7d) was associated with lightning activity less than 40 min before tornado formation and decaying shortly after. Other lightning clusters were larger in magnitude and duration, particularly those that arrived at the Maule Region, with one tornado reported that day in the town of Chanco (number 7 in Table 1 and Fig. 7d). Perhaps due to the mesoscale instability caused by the comma cloud, some convective cells and lightning activity lasted longer than 6 h on 31 May, with a similar storm direction (320°–330°) but greater magnitude (~20 m s<sup>-1</sup>) than the storms on 30 May.

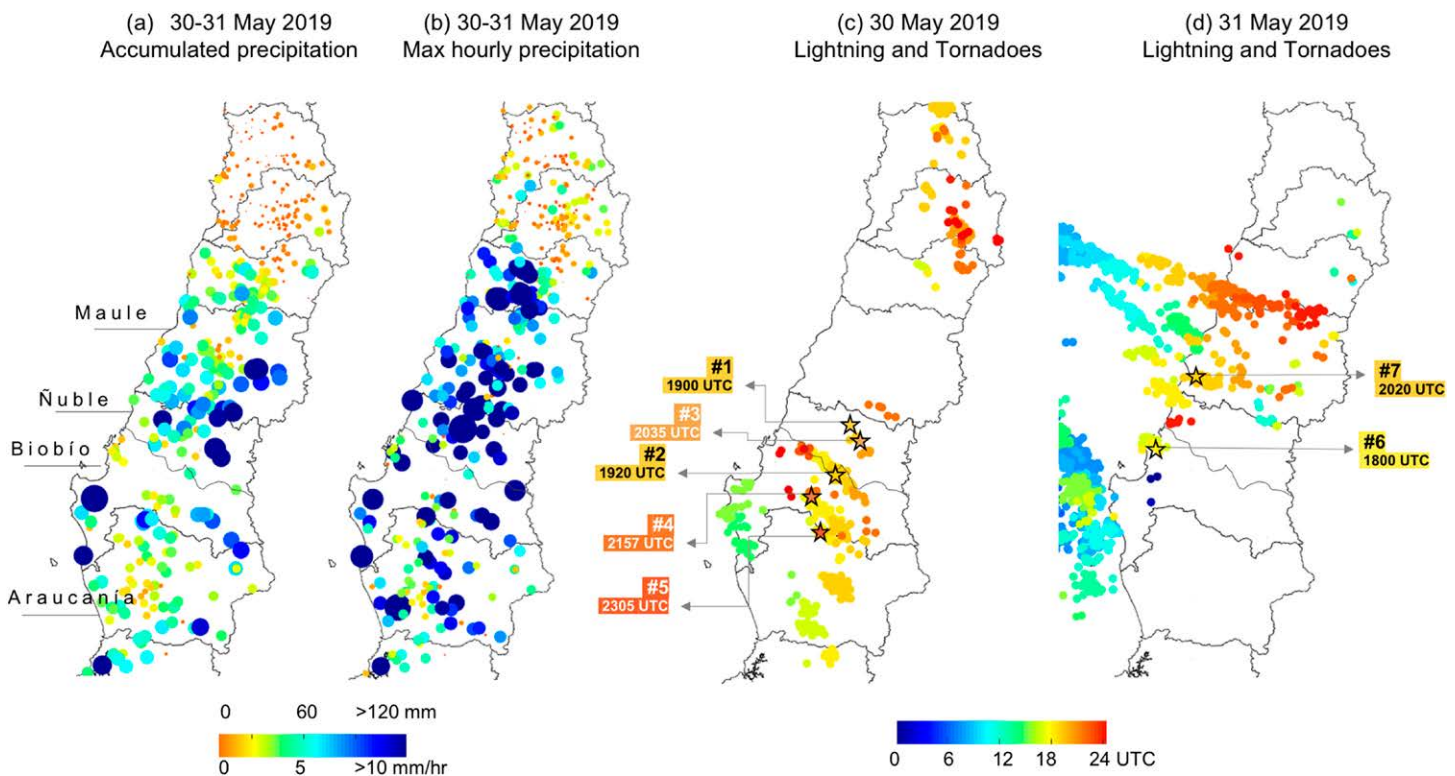


Fig. 7. (a) Total accumulated precipitation during 31 and 31 May 2019 (mm), (b) maximum hourly precipitation (mm h<sup>-1</sup>) observed during 30 and/or 31 May 2019, and lightning (colors) and tornado reports (black star) during (c) 30 May and (d) 31 May 2019. Tornado order (1–7) is also indicated according to the hour of occurrence (see Table 1).

**Wind shear and instability.** In this subsection, we track the local evolution of wind shear and instability given their crucial role in tornadic storms. Figure 8 (see also Fig. S3) shows instability and shear parameters calculated using WRF runs at the time of the two main tornadoes. During 2200 UTC 30 May 2019, the magnitude of low-level wind shear (0–1 km AGL) shows modest values over the ocean (between 5 and 10 m s<sup>-1</sup>) and much higher values inland (10–20 m s<sup>-1</sup>). However, differences in shear between land and ocean are insubstantial over the deeper 0–6 km AGL layer, suggesting a synoptic-scale or topographic origin for the deep shear. The inland low-level shear increase is partly due to weaker surface wind speeds over land (relative to offshore values) likely induced by differential friction. A more



pronounced northerly component is also present at 1 km AGL that may be related to the topographic blocking of the Andes and coastal cordillera (Kalthoff et al. 2002; Barrett et al. 2009; Barrett et al. 2020; Marín et al. 2020). The near-surface northeasterly winds are almost perpendicular to the southwesterly winds at 6 km AGL (Figs. 8a,c), thus maximizing the directional wind shear. This resembles the situation during tornadic storms in California and other regions of complex topography (Monteverdi et al. 2003)

As described above, on 30 May, CAPE from reanalysis reached only moderate values of 200–400 J kg<sup>-1</sup> approaching the continent from the ocean due to the prevailing midlevel westerly flow transporting cold air pockets. WRF simulations, which provide a higher resolution of the instability field, show a narrow structure of much higher CAPE along the Central

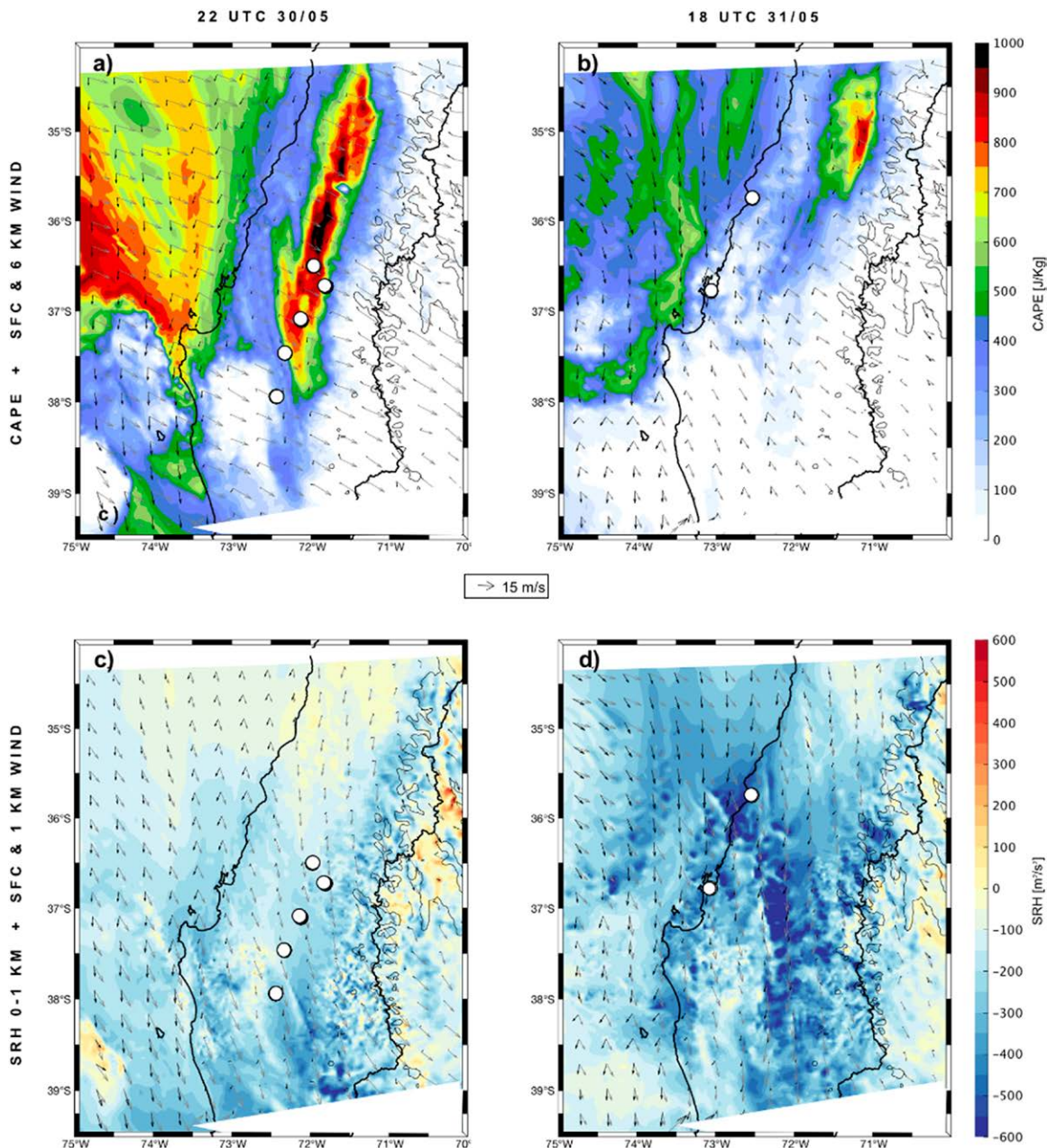


**Fig. 8.** (a),(b) The most unstable CAPE (shaded colors), surface wind (black arrows), and 6-km winds (gray arrows). (c),(d) SRH 0–1 km (shaded colors), surface wind (black arrows), and 1-km winds (gray arrows). Panels (a) and (c) correspond to 2200 UTC 30 May and (b) and (d) to 1800 UTC 31 May 2019. Tornado locations are plotted in white circles. The Andes Cordillera area is plotted in thin black contours (>3-km height above sea level). Data are from WRF simulations using 1-km horizontal resolution domain.

Valley between 34° and 38°S with values of up to  $1,000 \text{ J kg}^{-1}$  at the time of the tornado in Los Angeles (Fig. 8a). From AMDAR temperature and wind vertical profiles and WRF dewpoint temperature for Talcahuano–Concepción, we were able to construct skew  $T$ –log $p$  diagrams and calculate severe weather parameters from the hodographs for available flights during 30 May and 31 May using the SHARPPy toolkit (Blumberg et al. 2017, Fig. 9). The available AMDAR flight for 2052 UTC 30 May features a most unstable CAPE of  $673 \text{ J kg}^{-1}$ , consistent with values above  $500 \text{ J kg}^{-1}$  near the coast. Temperatures in the Central Valley were slightly higher

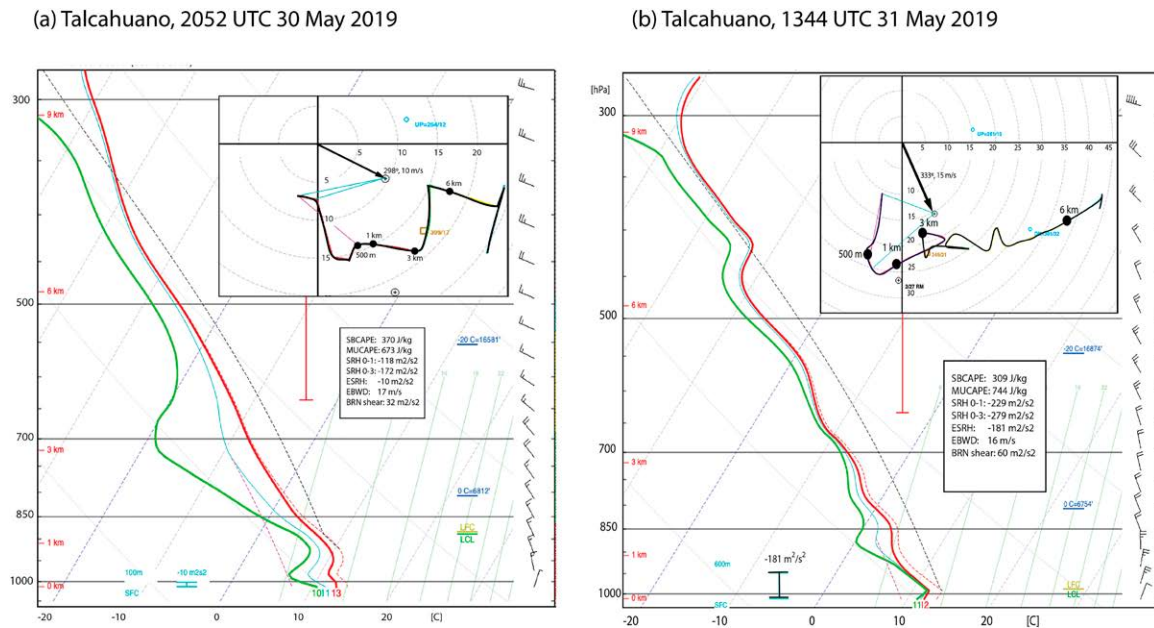


**Fig. 9.** Skew  $T$ –log $p$  diagrams and hodographs for the AMDAR profiles of (a) 2052 UTC 30 May 2019 and (b) 1344 UTC 31 May 2019 at Talcahuano, adapted from SHARPPy (Blumberg et al. 2017). The red line is the temperature profile, and the green line is the dewpoint (humidity is taken from WRF to construct these profiles). The hodographs show the storm motion for the left-mover storm (arrows; Bunkers et al. 2014). Black dots in the hodograph mark 500 m, 1 km, 3 km, and 6 km AGL. The insets show the values of several typical supercell parameters, as calculated by SHARPPy for each sounding.

than those near the coast where the profile was taken, reaching  $15^{\circ}$ – $16^{\circ}\text{C}$  in most stations prior to the initiation of convection. If the surface temperatures and humidity in Talcahuano are replaced by those of the Central Valley before the thunderstorms ( $T = 15^{\circ}\text{C}$ ,  $T_d = 13^{\circ}\text{C}$ ), one can easily reach surface CAPE values over  $1,000 \text{ J kg}^{-1}$ . This shows that CAPE is highly sensitive to even small variations in surface temperature (an increase of about  $500 \text{ J kg}^{-1} \text{ }^{\circ}\text{C}^{-1}$ ), indicating even moderate surface warming during the afternoon as a possible source of these high CAPE values. This is also supported by WRF simulations that show maximum CAPE over the Central Valley simultaneously with the maximum surface temperatures. Rapid destabilization by surface warming has been identified as a key factor in the severity of low-CAPE, high-shear storms in southeastern United States (King et al. 2017).

A widely used measure that indicates a storm’s likelihood of becoming supercellular is the storm-relative helicity (SRH) near the surface (Davies-Jones 1990; Rasmussen 2003). Figure 9 shows this quantity for 30 May near the time of the tornadoes in the Central Valley. Large values of 0–1-km SRH (calculated from the left-moving Bunkers’ storm motion) range from  $-100$  to  $-250 \text{ m}^2 \text{ s}^{-2}$  over the regions in which tornadoes occurred, which are within the typical tornadic storm range in continental United States (Rasmussen 2003; Thompson et al. 2007). AMDAR hodograph for that particular day taken at Talcahuano near



the coast (Fig. 8b) confirms a relatively large value of SRH 0–1 km of about  $-118 \text{ m}^2 \text{ s}^{-2}$ , largely explained by the 0–500-m layer. It is also remarkable that the hodograph exhibits most tornadic hodographs features (Esterheld and Giuliano 2008): a nearly straight-line shear vector in lower levels (about  $9 \text{ m s}^{-1}$ ) with a kink in lower levels at about 300 m, and a surface storm relative flow vector oriented nearly orthogonal to the low-level shear, which is the ideal situation for mesocyclone development in which low-level inflow contributes mostly to streamwise vorticity.

On 31 May, WRF simulates moderate CAPE levels off the coast ( $\sim 0\text{--}600 \text{ J kg}^{-1}$ , Fig. 8d) with smaller values over the Central Valley, except for an isolated maximum near  $35^\circ\text{S}$ . Greater instability values over the ocean appear connected to the comma cloud mesoscale low described in the “Synoptic-scale environment” section. The AMDAR profile in Talcahuano four hours before the tornado confirms relatively high unstable CAPE values of  $744 \text{ J kg}^{-1}$  and surface-based CAPE of  $309 \text{ J kg}^{-1}$  (Fig. 9). Both the surface and 1 km AGL winds increase substantially from the previous day, resulting in a longer hodograph with a maximum wind near 800 m of about  $25 \text{ m s}^{-1}$ . The corresponding AMDAR hodograph for Talcahuano at 1344 UTC (Fig. 9) shows an even higher SRH value of  $-229 \text{ m}^2 \text{ s}^{-2}$ , again with most of the contribution coming from the layer below 500 m. In this particular case, the tornadic features of the hodograph are even more striking than those of the previous day. Besides the larger SRH values, the angle between relative inflow and low-level shear (critical angle parameter) is almost orthogonal ( $82^\circ$ ). WRF fields of 0–1 km AGL SRH provide a spatial context for this individual observation. At 1800 UTC 31 May (Fig. 8d), values around  $-200 \text{ m}^2 \text{ s}^{-2}$  are widespread with localized patches of even  $-600 \text{ m}^2 \text{ s}^{-2}$  near the coast and along the Central Valley, roughly coinciding with the location of the observed tornadoes during this day.

Based on analysis of a large contiguous U.S. tornado database, Coffey et al. (2019) argue for the use of 0–500-m SRH as the best discriminant between tornadic and nontornadic storms, finding that significant tornadoes appear with mean SRH magnitudes of about  $220 \text{ m}^2 \text{ s}^{-2}$ . For 31 May, the AMDAR profile shows an SRH between 0 and 500 m of about  $-160 \text{ m}^2 \text{ s}^{-2}$ ; however, if one replaces the calculated storm motion with the actual storm motion observed from GOES infrared (GOES-IR), SRH 0–500 m rises to about  $-200 \text{ m}^2 \text{ s}^{-2}$ , a magnitude well above the no-tornado interquartile range and more typical of the weak and significant tornado categories in Coffey et al.’s (2019) analysis. By inspecting the WRF simulations, we see that the highest SRH values are associated with the propagation of the comma cloud structure eastward toward the continent, which is far less organized in WRF than in GOES infrared imagery. However, one can speculate that near-surface baroclinicity present at the surface front of the comma cloud structure could enhance the low-level shear by thermal wind balance and thereby favor tornadogenesis on 31 May. The absence of a similarly organized mesoscale structure on 30 May may explain that day’s relatively weaker SRH values (Figs. 8b,d).

**Storm evolution from GOES-IR.** The storm that originated the tornado in Los Angeles (30 May) was one of five that formed during the evening of 30 May over the moderate CAPE region within the Central Valley. GOES infrared images show the initiation of the storm at about 2127 UTC (thin black contour in Fig. 10a) about 20 km northwest of the tornado. As the storm moved southeasterly, severe weather was reported near Los Angeles, including large hail ( $>2\text{-cm}$  diameter; Fig. S2a), heavy rain, and lightning starting about 20 min before tornadogenesis (see Fig. 2c). Around 2157 UTC, a tornado is observed in northeastern Los Angeles, located in the rear (upshear) poleward quadrant relative to the storm’s center following a mostly north–south trajectory (dashed line in Fig. 10a). The tornadic storm develops a secondary region of ascent 10 min later (2207 UTC) in the same quadrant in which the tornado was located (in Fig. 10a, cloud tops lower than  $-46^\circ\text{C}$  are plotted in gray lines). The convective cell lasted around 3 h in total from first sight in the IR images at 2000 UTC until no updraft

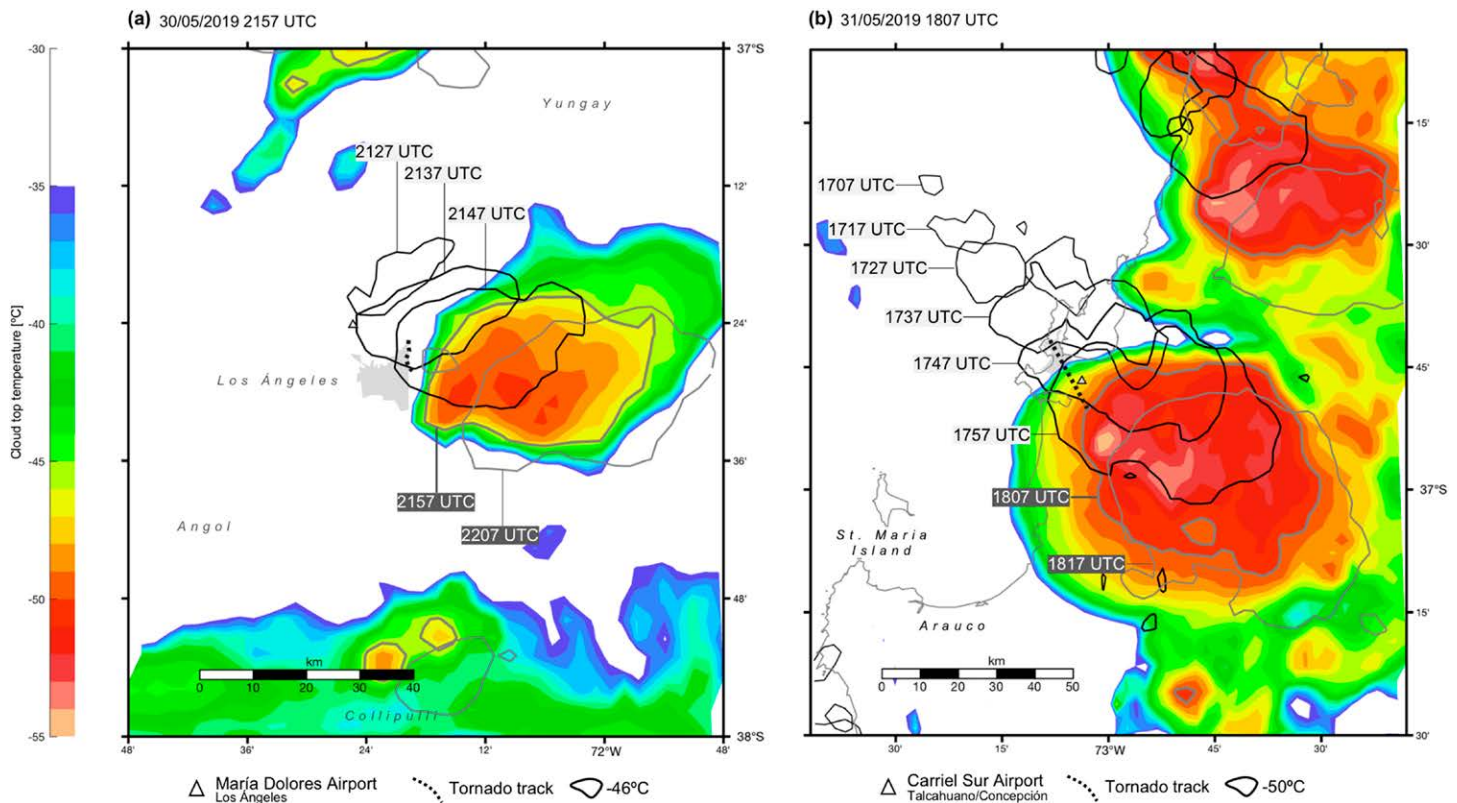


**Fig. 10.** Cloud-top temperature from infrared satellite image (channel 13, *GOES-16*; °C; color shaded) at the tornado moment: (a) 2157 UTC 30 May for Los Ángeles and (b) 1807 UTC 31 May for Talcahuano–Concepción. We also plotted the storm evolution considering the cloud-top temperatures of  $-46^{\circ}\text{C}$  in (a) and  $-50^{\circ}\text{C}$  in (b) every 10 min before the appearance of the tornadic storm, in black contours, and after the tornado, in gray contours. The dashed black line corresponds to the tornado path at the surface. Light gray areas represent urban zones, corresponding to Los Ángeles in (a) and Talcahuano–Concepción in (b). Triangles can also help to reference the cities' positions: María Dolores Airport of Los Ángeles in (a) and Carriel Sur Airport of Talcahuano in (b). Data were obtained from [http://home.chpc.utah.edu/~u0553130/Brian\\_Blaylock/cgi-bin/goes16\\_download.cgi](http://home.chpc.utah.edu/~u0553130/Brian_Blaylock/cgi-bin/goes16_download.cgi).

could be identified at 2300 UTC. Given the top brightness temperature as an indication, the depth of the convective storm was around 9 km. Following the motion of the updraft in the GOES images, a storm motion vector of  $328^{\circ}$  and  $12\text{ m s}^{-1}$  may be derived.

Figure 10b tracks the evolution of the storm that affected Talcahuano–Concepción on 31 May. Between 1700 and 1800 UTC, the storm increased, with around 20 lightning flashes identified by WWLLN before 1730 (Fig. 7d). Once the convective system was inland, the tornado had already commenced its path over the city at 1800 UTC. Again, the tornado is located in the rear poleward (rear-right) quadrant of the storm relative to the motion of the coldest cloud top. The observed trajectory of the tornado closely follows the trajectory of the coldest cloud top separated by about 15 km, indicating the tornado's position relative to the center of the updraft.

In the absence of radar data, some observational indications that tornadoes were embedded within supercellular storms can be gained from the *GOES-16* satellite images (Fig. 10, Table 1): most storms have minimum brightness temperatures near 215 K (corresponding to a height between 12 and 15 km according to soundings 500 km south and north of Concepción), an indication that overshooting tops reached the tropopause on 31 May, sometimes developing characteristic enhanced-V, cold-U signatures and nearby warm areas in the anvil (Fujita 1982; Adler et al. 1981; Moller et al. 1994; Brunner et al. 2007; Peyraud 2013). Some storms showed a flanking line, characteristic of classic supercells (Moller et al. 1994). In all seven tornadoes, the overshooting tops in the infrared images are located close to the tornadoes at the surface



(Lemon and Doswell 1979; Markowski and Richardson 2011) in the rear flank of the cell (relative to the storm's motion). The tornadoes of Talcahuano–Concepción and Los Ángeles (see Fig. 10) are located about 10 km away from the updraft, in the region of brightness temperature warmer than  $-35^{\circ}\text{C}$  and along the storm motion's direction. As suggested by B. Barrett (2020, personal communication), this may be interpreted as a strongly sheared updraft and a further indication of these storms' supercellular nature.

Common to other tornadic storms described in the literature, the time evolution of the overshooting top in the infrared indicates a rapid cooling between 50 and 10 min before the appearance of a tornado at the surface followed by a relative warming of the updraft region at the time of tornadogenesis (see Peyraud 2013, and references therein). The IR features found in each of the storms are summarized in Table 1.

Additional evidence for supercellular tornadogenesis comes from videos and pictures of the two main tornadoes that show the existence of a cloud wall surrounding the tornadoes while clear slots attest the parent mesocyclone and rear downdraft (Fig. S2b). The duration of the cells (2–3 h) and the size derived from the infrared are also characteristic of supercells. Higher resolution numerical simulations and analysis of the propagation of the Los Ángeles and Concepción cells performed by Barrett et al. (2020), in addition to our own, give further credence to the supercell nature of the tornadic storms. Storm motion of the left-moving supercell calculated using the SHARPPy toolkit (Bunkers et al. 2014; Blumberg et al. 2017) confirms the storm motion derived for each tornado based on GOES-IR observations (Table 1).

### Severe storm environment for tornadoes in Chile

**Seasonal and geographical distribution of historical tornadoes.** From 1633 to 2019, at least 43 tornadoes were reported in central and southern Chile, comprising a database created and constantly updated by the Chilean Navy Weather Service (Servicio Meteorológico de la Armada 2010) and DMC in recent years (Fig. 1). As described by Alonso de Ovalle in one of the first chronicles of colonial life in Chile (de Ovalle 1703), on 14 May 1633, the Spanish fortress town of Carelmapu was almost completely destroyed by a tornado (see circle around  $42^{\circ}\text{S}$  in Fig. 1). The description is so vivid that it even contains information about the size of hail “without exaggeration ... thicker than larger musket balls,” which translates to about 2–4-cm diameter, or a sedimentation velocity of about  $20\text{--}30\text{ m s}^{-1}$ . Hail of similar size was reported on social networks during the May 2019 storms near the Los Ángeles tornado (Fig. S2a). A better-known historical tornado crossed Concepción on 27 May 1934, causing considerable damage along a northwest–southeast trajectory. This storm was covered by the *New York Times*, indicating damage worth 1 million dollars at the time (*New York Times*, 29 May 1934). From 2000 to the present, reports of about 40 different tornadoes and waterspouts (86% of total observations) can be found in the press and social media. As Fig. 1 illustrates, tornado reports have increased toward southern Chile, reaching a maximum density near  $37^{\circ}\text{S}$  (Ñuble and Biobío regions) and around  $41^{\circ}\text{S}$  (Los Lagos region). Sixty-nine percent of all recorded tornadoes occurred between 2015 and 2019. Increased social network use and high cell phone coverage, even in rural areas, may explain the apparent recent prevalence of tornadoes in Chile. Alternatively, the increase in tornado reports could be a real climate signal associated either with recent natural decadal variability or anthropogenic climate change, which are known to be at play in recent drying trends over the same region (Boisier et al. 2016).

Another important feature is that the maximum frequency occurs during fall and winter, denoted by pale blue and blue dots in Fig. 1. The peak frequency occurs during fall with 17 tornadoes reported (46%) followed by winter season with 16 tornadoes (43%). Most tornadoes occurred during the month of May, including those from Carelmapu and Concepción in 1633 and 1934 and the 2019 outbreak, mirroring the seasonality found in southwest Australia,

California, and England, where the maximum frequency occurs during the cool season (Blier and Batten 1994; Hanstrum et al. 2002; Kirk 2014).

**CAPE and shear.** This subsection aims to contextualize the late May 2019 tornadic storms more broadly and to examine how exceptional the dynamical and thermodynamic conditions concurrent with their development were. We begin by considering the large-scale environment that form rainstorms in south-central Chile using reanalysis to characterize the shear and instability environments of severe storms, as earlier studies have (e.g., Brooks 2009; Taszarek et al. 2018). These synoptic conditions are synthesized in Fig. 11. Relative to dry days (black dots), those days with more than 1 mm of rainfall (gray circles) exhibit higher most unstable CAPE ( $10\text{--}50\text{ J kg}^{-1}$ ) and higher bulk shear values ( $5\text{--}10\text{ m s}^{-1}$ ) in connection with stronger-than-average winds aloft. CAPE and shear exhibit some positive correlation, and the precipitation amount (reflected in the symbol size) tends to increase with both low-level wind shear and CAPE. Let us now examine the synoptic conditions during lightning storms as an indicator of unstable conditions. Given the formation mechanism of electrical strokes in the atmosphere, lightning activity tends to increase with convective rainfall and other storm metrics (Pessi and Businger 2009). Over the central United States, strokes almost double in frequency in tornadic storms relative to nontornadic storms (Turman and Tettelbach 1980). Consistent with the mostly stable nature of the cold frontal systems, lightning occurrence along the Chilean coast is notoriously low except for a well-defined maximum in western Patagonia (south of  $42^{\circ}\text{S}$ ; Garreaud et al. 2014). For the present study, we consider a  $3^{\circ} \times 3^{\circ}$  box centered at  $37^{\circ}\text{S}$ ,  $72.5^{\circ}\text{W}$ , thus encompassing the cities of Concepción and Los Ángeles in the Biobío region. Only 47 days in the 11-yr record have more than 25 WWLLN strokes (“Data” section), including 30 and 31 May 2019 (with 84 and 239 strokes, respectively). The corresponding CAPE–SHEAR values for 30–31 May 2019 are highlighted (orange and red circles) in Fig. 11a. CAPE values are similar on both days ( $100\text{--}200\text{ J kg}^{-1}$ ; notice that these are daily means of ERA5 reanalysis) and within the upper tail of the distribution. Likewise, the wind shear values are also similar (about  $15\text{ m s}^{-1}$ ) and well above the interquartile range of lightning storms. The CAPE–wind shear values of the other three tornadic storms in this region are also in the upper parts of their respective distributions (Fig. 11a). From this simple analysis, we infer that substantial CAPE values are a necessary condition for the occurrence of tornadic storms in south-central Chile; however, these values do not differ significantly from those of lightning storms. If we consider the five tornadic storm days shown in Fig. 11a, this subset exhibits low-level wind shear values (higher than about  $12\text{ m s}^{-1}$ ), well above the typical range of rainy or even thunderstorm days for the region.

**Low-level vorticity generation parameter.** Motivated by the fact that the generation of vertical vorticity by tilting of horizontal vorticity is proportional to the updraft speed times the magnitude of the vertical shear (e.g., Rasmussen and Blanchard 1998; Markowski and Richardson 2011), authors have attempted different combinations of shear and CAPE to discriminate between severe and nonsevere thunderstorm environments. For instance, Brooks (2009) shows probabilities of severe thunderstorms as a function of mixed-layer CAPE and 0–6-km wind shear, concluding that even the simple product of the two can be a valuable forecasting parameter.

Rasmussen and Blanchard (1998) noted that, within parcel theory, the maximum velocity of an updraft is proportional to  $\sqrt{\text{CAPE}}$ , and given that vertical shear of the horizontal wind is the main contributor to horizontal vorticity, they defined the low-level vorticity generation parameter (VGP;  $\text{m s}^{-2}$ ) as the product of  $\sqrt{\text{CAPE}}$  and the mean shear between 0 and 4 km. VGP has appeared in the recent literature under other terminology and with different physical units: for instance, Tsonevsky et al. (2018) calculate shear between the 925- and 500-hPa



ERA5 daily mean March 2008 - September 2019  
(March to September only)

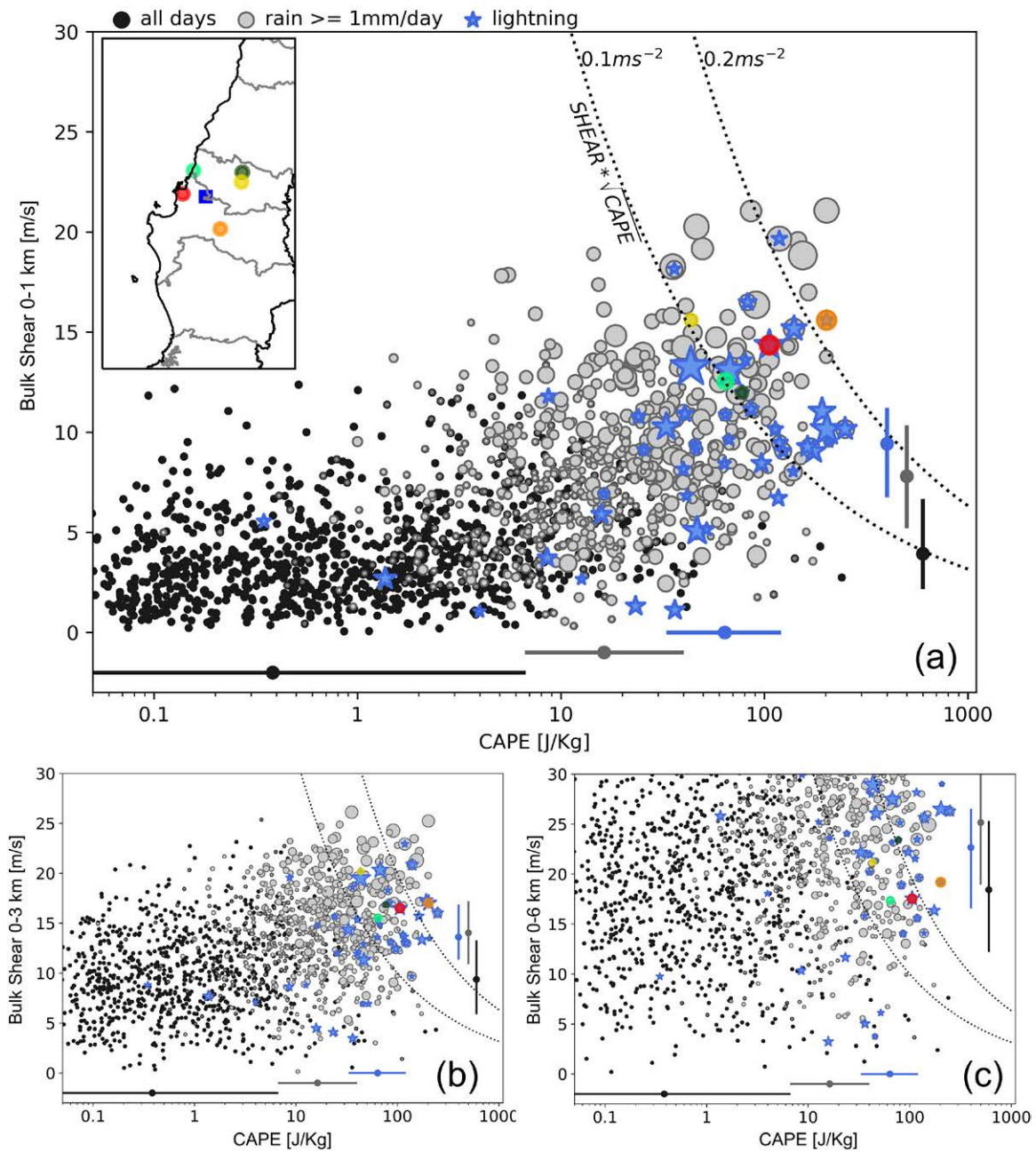


Fig. 11. Instability–shear joint distribution over the Biobío region. Each symbol represents one day during fall–winter (March–September) from 2008 to 2019. The horizontal axis is the daily mean most unstable CAPE (note the logarithmic scale), and the vertical axis is the daily mean magnitude of the wind shear in a column centered at 37°S, 72°W (blue square in inset, halfway between Concepción and Los Ángeles) between the surface and (a) 1, (b) 3, and (c) 6 km AGL. Daily means are computed from hourly ERA5 data. Black circles are dry days, gray circles are rainy days (>1 mm in the central box) with their size proportional to daily accumulation (the larger circles are about 70 mm day<sup>-1</sup>), and blue stars are days with more than 25 WWLLN lightning strokes in a 3° × 3° box centered at 37°S, 72.5°W, with their size proportional to daily number. Black, gray, and blue lateral bars (dots) indicate the interquartile range (median) of CAPE–shear during dry, rainy, and lightning days, respectively. The conditions on 30 and 31 May 2019 are identified by the orange and red circles, respectively. Dotted lines indicate lines of constant 0–1-km shear times square root of CAPE ( $m s^{-2}; VGP_{0-1}$ ).

pressure levels and call the product with CAPE “CAPE–SHEAR” or “CAPES,” suggesting that it is a better predictor of severe weather in high-shear, low-CAPE environments. VGP may be considered a simple way to consider instability and wind shear to evaluate the possibility that an environment will generate vertical vorticity by tilting, which is regarded as the physical process responsible for the formation of a midlevel mesocyclone within a supercell thunderstorm (Markowski and Richardson 2011). Although the formation of a supercell is known to be favored by the deep-layer shear (typically 0–6 km), low-level shear (between the surface and 1 km AGL) seems to be instrumental for the mesocyclone’s ability to produce strong low-level vertical accelerations and provide the correct alignment between the mesocyclone and surface-vertical vorticity (Coffer and Parker 2017; Guarriello et al. 2018; Sherburn and Parker 2019), which favors tornadogenesis. This has led authors to propose even shallower layers for the calculation of severe weather parameters, such as the SRH (Coffer et al. 2019) to distinguish ordinary from tornadic supercells. Following these arguments, we calculate here a low-level VGP as a discriminant between tornadic and nontornadic storms in our region. Figure 11a shows two isolines of the product of  $\sqrt{\text{CAPE}}$  and 0–1 km AGL shear from reanalysis ( $\text{VGP}_{0-1}$ ). The five tornado days found in the study region and period show values of  $\text{VGP}_{0-1}$  greater than  $0.1 \text{ m s}^{-2}$ , and the stronger tornado of Los Angeles is within the  $0.2 \text{ m s}^{-2}$  isoline (partly helped by one of the highest CAPE values within the entire period considered). For the limited number of cases available, these thresholds appear to be a useful first-order discriminant. Thresholds are, of course, highly dependent on the time and space resolution of the analysis used to construct them, as attested by the much higher most unstable CAPE values in our WRF simulations compared to the ERA5 reanalysis. As in other cold-season cases, deep-layer shear offers little discriminating power since deep shear is usually available during winter at this extratropical latitude. This can be seen in CAPE–SHEAR scatterplots for deeper levels (Figs. 11b,c) where more storms (and even dry cases) can have shear values comparable to those in tornadic situations. Given the proximity to the coast and available humidity, other parameters deemed important in the United States, such as the lifting condensation level, also appear less critical for this region.

## Summary

In this final section, we summarize the main synoptic, mesoscale, and historical aspects of tornadoes in Chile, considering the late May 2019 outbreak. At least seven tornadoes were reported between 30 and 31 May 2019, in a historical tornado hotspot in the area (around  $37^\circ\text{S}$ ), matching the peak frequency observed in previous reported tornadoes during late fall.

Tornadic storms were promoted by the presence of a blocking anticyclone off austral Chile and a quasi-stationary low farther north, and a cold air advection around  $35^\circ$ – $37^\circ\text{S}$  at mid- and high levels of the troposphere. The location of the quasi-stationary low near the surface was such that warm air advection along the coast between  $35^\circ$  and  $40^\circ\text{S}$  enhanced instability over a period of about four days. The interaction between the unstable air above the low and the passage of midlevel shortwaves traveling along the enhanced subtropical jet, initiated convection over the Central Valley of southern Chile on 30 May 2019 and on a more organized quasilinear band of convection associated with a comma cloud on 31 May 2019 (see schematic in Fig. 12).

Based on mesoscale simulations conducted with WRF, instability peaked several hours before the tornado reports with most unstable CAPE values ranging between 500 and  $1,000 \text{ J kg}^{-1}$ . AMDAR profiles taken at Talcahuano–Concepción airport agree with these values of instability, showing that about half of the CAPE is contained in the lower 4 km of the sounding. Relatively large values of SRH related to high low-level shear values were present during the 2-day outbreak, based on WRF simulations and AMDAR profiles. Severe weather, including large hail and lightning activity, was present between 20 and 40 min before each tornado



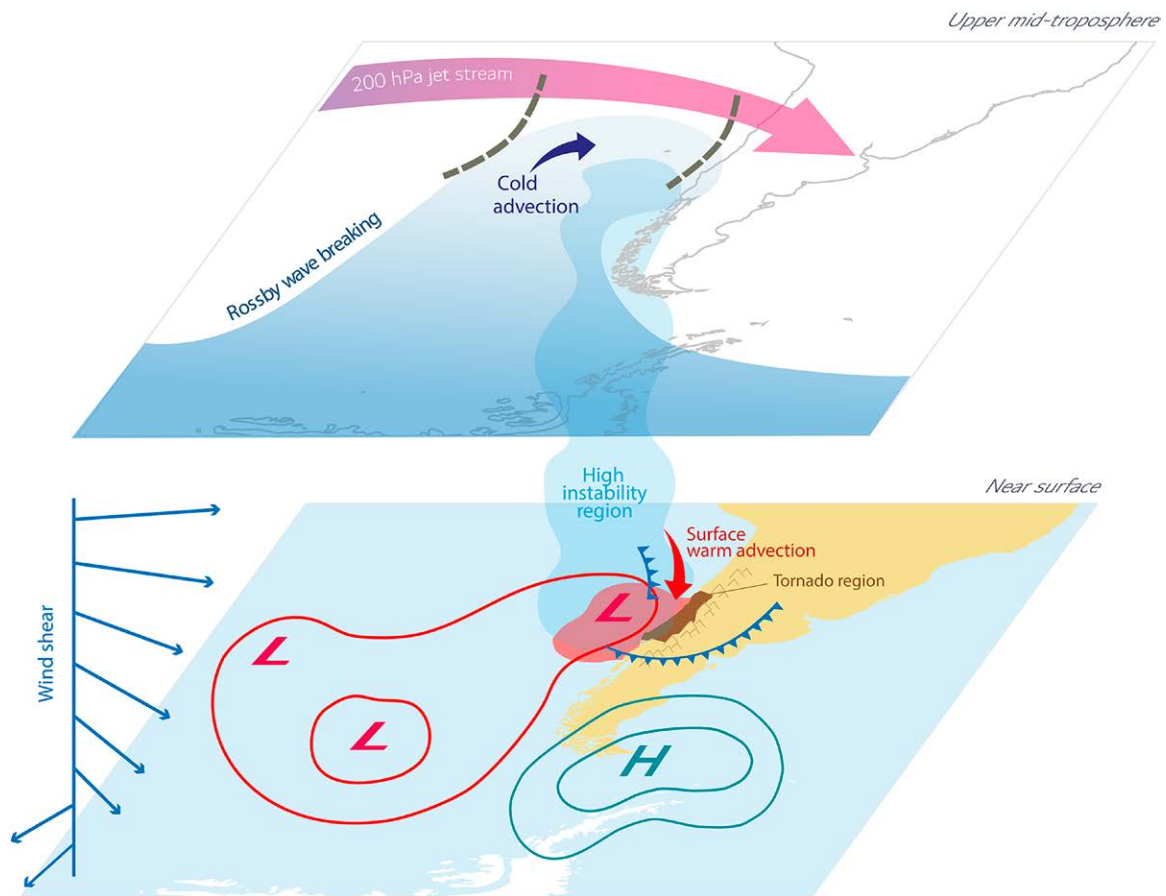


Fig. 12. Conceptual model summarizing synoptic main features of tornadic storms during the May 2019 outbreak. (top) Dynamical features of the upper and midtroposphere, highlighting the position of the jet stream, cold advection, short waves (dashed lines), and Rossby wave breaking. (bottom) Dynamical features near the surface, highlighting the wind shear profile, surface warm advection, position of the blocking high (H), and low pressure centers (L).

sighting. Inspection of *GOES-16* infrared images reveals several characteristics observed in supercellular tornadic storms: the development of a single overshooting that suffers a relative warming 20–10 min before tornadogenesis; enhanced-V, cold-U signatures; flanking lines; and an apparent sheared updraft, by contrasting the surface tornado's position with that of the corresponding updraft. The storm motion derived from *GOES-IR* for the seven tornadoes closely follows the storm motion derived from the *AMDAR* profiles for the left-moving storm, as would be expected from supercells in the Southern Hemisphere.

Although CAPE values are relatively low compared to those found in the world's main areas of severe convection (U.S. Great Plains, Argentina), they are extraordinary for southern Chile climatology. On the other hand, low-level shear values are comparable to the ones in most tornadic regions of the world. Revisiting earlier literature on cold-season tornadoes in Australia and California (Monteverdi et al. 2003) and on the basis of our own analysis and that of Barrett et al. (2020), we found that Chilean tornadoes conform to the major synoptic-scale ingredients described as environmental factors that favor the occurrence of tornadoes during the cold season on other continents: strong low-level wind shear, moderate values of instability, and the presence of a diffluent trough in midlevels equatorward of a midlatitude cyclone and close to the coast, among others (Hanstrum et al. 2002). Recent discussion in the literature points to the critical role of low-level shear both in the generation of the mesocyclone (and therefore the supercell) and in the generation of tornadogenesis once the mesocyclone is established. Even for our limited sample of cases, the May 2019

tornado outbreak seems to support this view: observations taken before the Talcahuano tornado show particularly large low-level shear values and, more specifically, large SRH values concentrated in a shallow layer near the surface. Despite the large shear and SRH values, indices such as the significant tornado parameter (e.g., Blumberg et al. 2017) would not have produced tornado alarms for our case, perhaps by giving too much weight to CAPE values compared to shear and SRH. Given the low frequency of these events, refining the parameters for predicting environments favorable for tornado occurrence under low-CAPE, high-shear conditions may require the synthesis of worldwide available observations under low-CAPE, high-shear environments in a single dataset. In the meantime, low-level VGP emerges as a useful metric to synthesize relevant ingredients (shear and CAPE) for tornado occurrence from our limited sample of cases. In the absence of nearby radiosonde stations and radar, we show that AMDAR profiles provide useful and critical information that may be used in real time for severe weather warnings.

**Acknowledgments.** C.B. and R. A. acknowledge the Chilean National Weather Service for funding a field reconnaissance visit to obtain information about the destruction caused by the Talcahuano–Concepción and Los Ángeles tornadoes and for the WRF simulations used in this research. We appreciate the contribution of the National Emergency Office from Ñuble region for confirming the information on the tornadoes in Yungay, San Carlos, and Coihueco. GOES data were provided by NOAA via Amazon Web Services. R.R., R.V. and R.G. acknowledge funding from FONDAP-ANID 151110009. R.R. also acknowledges funding from FONDECYT-ANID 1181781. We appreciate comments and suggestions by Brad Barrett and two anonymous reviewers that helped to improve the content and presentation of the manuscript.

### **Appendix: Tornado path and surface data**

The tornado that affected Los Ángeles on 30 May was first observed at 2157 UTC over the northeastern part of the city (Fig. 8a) moving southward from a rural sector and entering the urban area around 2200 UTC. Damage occurred along a 5-km path over less than 10 min, completely destroying one factory, damaging dozens of houses' roofs, felling trees, overturning trucks, displacing cars and trucks by several meters, and injuring dozens (Table 1; Vicencio et al. 2019). Over 6,000 people were affected by power outages. The intensity of this tornado was estimated on the enhanced Fujita scale as an EF2, with maximum winds reaching 50–60 m s<sup>−1</sup>.

On 31 May, a second tornado crossed the country's second-largest city, known as Gran Concepción. The tornado was first observed by a commercial airplane pilot as a waterspout over the sea near the coast (C. Ponce 2019, personal communication), making landfall shortly after report at Caleta El Soldado around 1750 UTC (first black dot in Fig. A1b). The tornado's inland trajectory was about 15 km between Talcahuano and Concepción, with a total duration of 15 min (Fig. A1b). Most damage was observed over Talcahuano city (in the first half of the trajectory), including 50,000 people affected by power outages, roof damage to dozens of houses and factories, cars displaced by several meters, and one fatality, leading to intensity estimates ranging from EF1 to EF2 (Vicencio et al. 2019; Aránguiz et al. 2020).

The odds of a weather station sampling a tornado are very low (only a few dozen such cases have been reported for the United States in over 100 years (Karstens et al. 2010; Edwards et al. 2013); remarkably, the 31 May tornado over Talcahuano was measured at Carriel Sur Airport. Its northwest–southeast trajectory was located around 400 m from two automatic weather stations close to the airport runway (AVIMET and MIDAS in Fig. A2a). After 1800 UTC, both weather stations recorded an abrupt pressure drop, descending 2.1 hPa in 6 min at AVIMET and 1.9 hPa at MIDAS. The minimum pressure



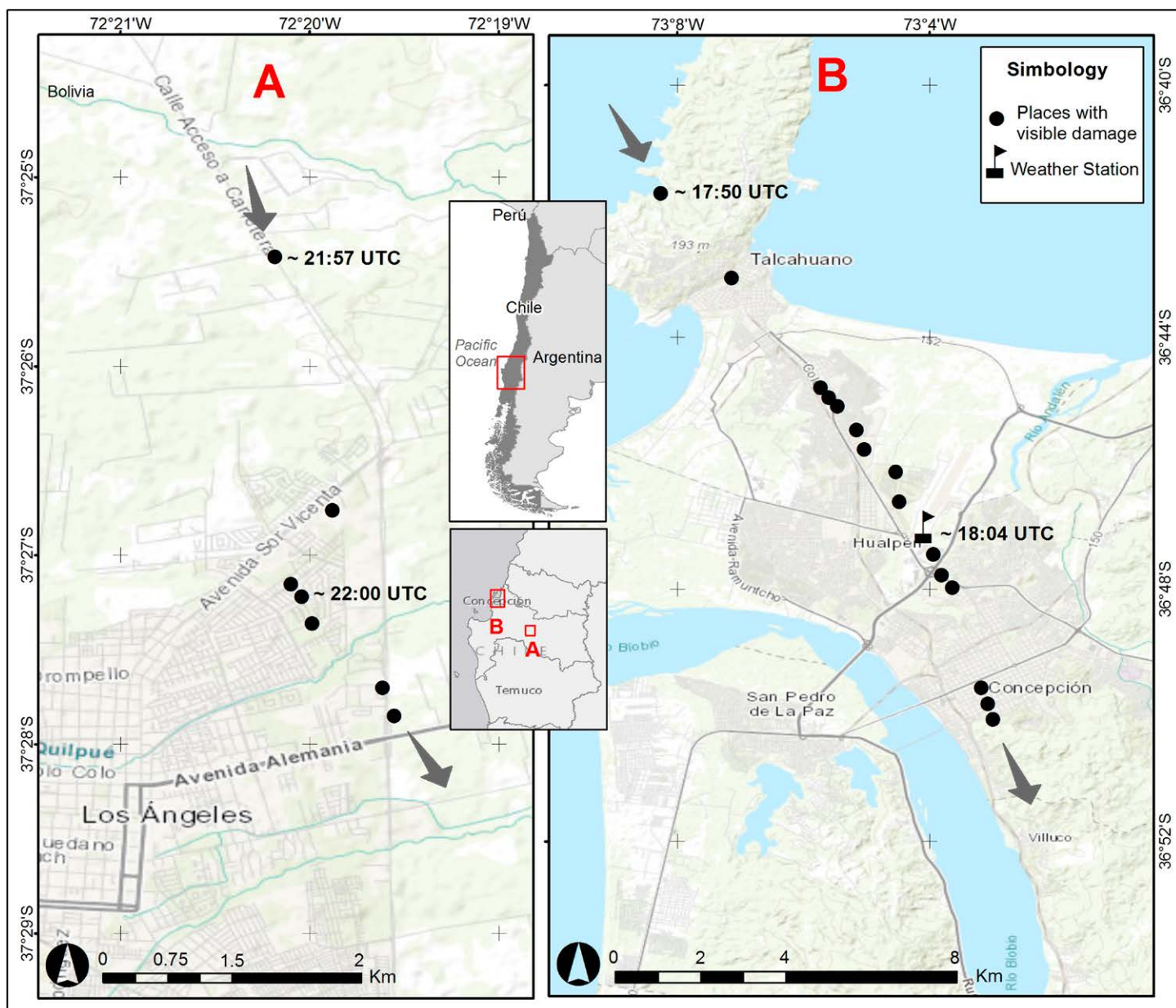
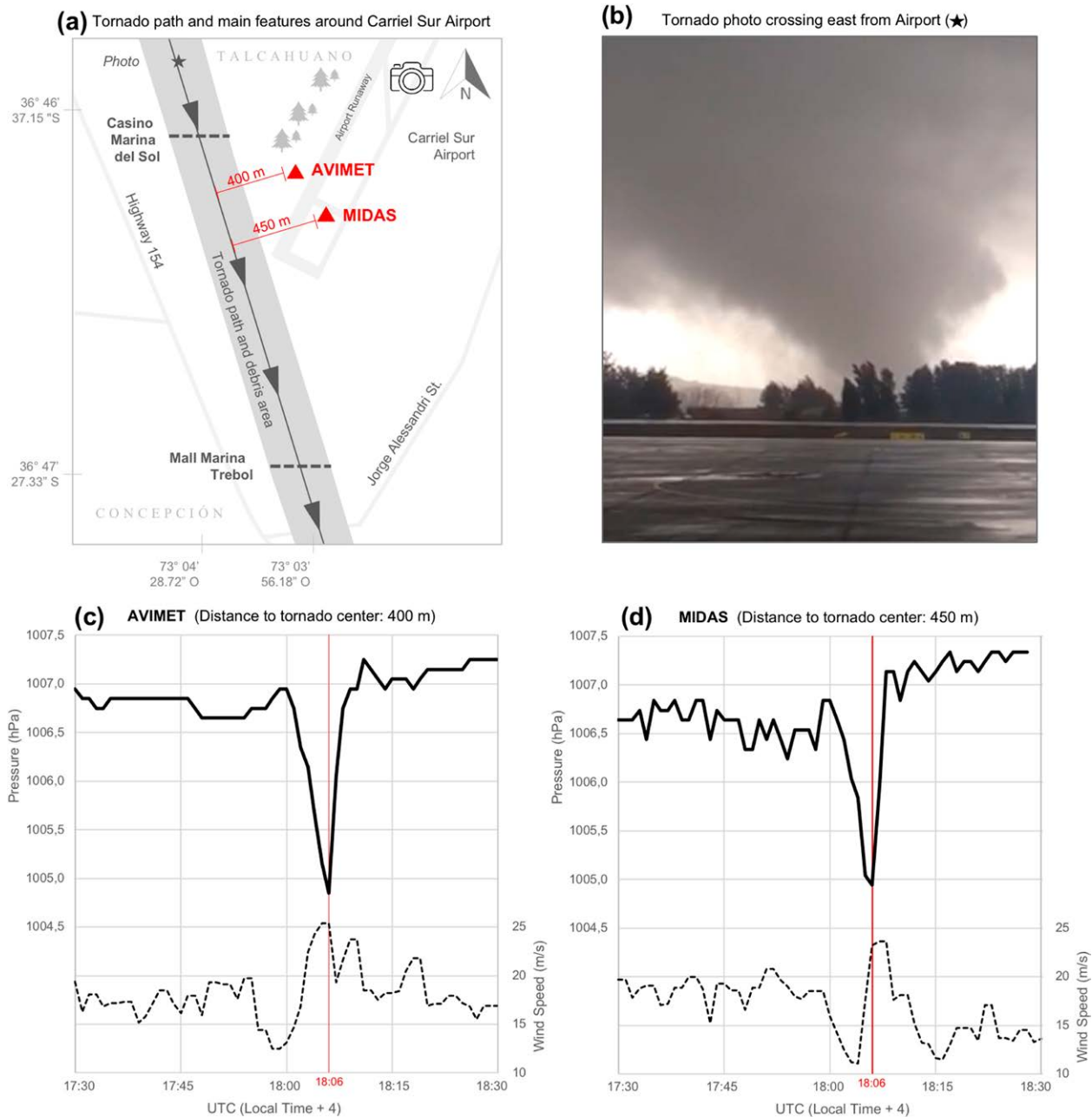


Fig. A1. Tornado trajectory and damage points reported in (a) Los Ángeles and (b) Talcahuano–Concepción, including the location of known affectionation hours in UTC. The flag symbol indicates the location of Carriel Sur Airport's weather station.

was observed simultaneously at 1806 UTC together with an initial decrease and subsequent increase in wind speed, reaching a maximum of  $24.4 \text{ m s}^{-1}$  at 1805 UTC on AVIMET and  $23.8 \text{ m s}^{-1}$  at 1806 UTC on MIDAS (bottom panels in Fig. A2). A picture taken from the runway of Carriel Sur Airport (Fig. A2b) shows the tornado touching the surface and moving toward the southeast several minutes before being measured by AVIMET and MIDAS weather stations.

Assuming that the maximum tangential velocity is located around 80 m from the center of the tornado (damage from the ground was estimated to occur over a maximum extension of about 150 m wide), this velocity may be estimated using theoretical profiles from the literature (Wood and White 2011). Parameters from Kato et al. (2015) give an estimate of  $50\text{--}55 \text{ m s}^{-1}$  for the maximum surface wind strength (upper EF1 or lower EF2 in the enhanced Fujita scale), consistent with the upper limit of intensity inferred from damage assessed in the field by the Chilean Weather Service (Vicencio et al. 2019) and with damage assessment developed by Aránguiz et al. (2020).



**Fig. A2.** (a) Tornado path (gray solid line), the estimated width according to the main debris area (shaded area), and principal features around Carriel Sur Airport, located between Talcahuano and Concepción, including two buildings with major damage (horizontal dashed line) and the location of two weather stations (red triangles). (b) A photograph of the tornado passing east from Carriel Sur after Casino Marina del Sol [taken by airport Dirección General de Aeronáutica Civil (DGAC) personnel from the landing track]. The camera symbol indicates the direction toward the star symbol in (a). (c) AVIMET and (d) MIDAS weather stations with measures of surface pressure (black solid line) and 10-m instantaneous wind speed (black dashed line), located 400 and 450 m from the tornado center, respectively.

## References

- Abarca, S. F., K. L. Corbosiero, and T. J. Galarneau Jr., 2010: An evaluation of the Worldwide Lightning Location Network (WWLLN) using the National Lightning Detection Network (NLDN) as ground truth. *J. Geophys. Res.*, **115**, D18206, <https://doi.org/10.1029/2009JD013411>.
- Adler, R. F., D. D. Fenn, and D. A. Moore, 1981: Spiral feature observed at top of rotating thunderstorm. *Mon. Wea. Rev.*, **109**, 1124–1129, [https://doi.org/10.1175/1520-0493\(1981\)109<1124:SFOATO>2.0.CO;2](https://doi.org/10.1175/1520-0493(1981)109<1124:SFOATO>2.0.CO;2).
- Aránguiz, R., B. Saez, G. Gutiérrez, C. Oyarzo-Vera, E. Nuñez, C. Quiñones, R. Bobadilla, and M. T. Bull, 2020: Damage assessment of the May 31st, 2019, Talcahuano tornado, Chile. *Int. J. Disaster Risk Reduct.*, **50**, 101853, <https://doi.org/10.1016/j.ijdrr.2020.101853>.
- Barrett, B. S., R. Garreaud, and M. Falvey, 2009: Effect of the Andes Cordillera on precipitation from a midlatitude cold front. *Mon. Wea. Rev.*, **137**, 3092–3109, <https://doi.org/10.1175/2009MWR2881.1>.



- , J. C. Marin, and M. Jacques-Coper, 2020: A multiscale analysis of the tornadoes of 30–31 May 2019 in south-central Chile. *Atmos. Res.*, **236**, 104811, <https://doi.org/10.1016/j.atmosres.2019.104811>.
- Bastias-Curivil, C., 2019: *Influencias de Los Procesos Geológicos En La Cosmovisión Mapuche, Entre Concepción Y Chiloé*. Undergraduate thesis, Facultad de Ciencias Físicas y Matemáticas, Universidad de Chile, 376 pp., <http://repositorio.uchile.cl/handle/2250/175020>.
- Berrisford, P., D. Dee, K. Fielding, M. Fuentes, P. Kallberg, S. Kobayashi, and S. Uppala, 2009: The ERA-Interim archive. ERA Rep. Series 1, 16 pp., <https://www.ecmwf.int/node/8173>.
- Blier, W., and K. A. Batten, 1994: On the incidence of tornadoes in California. *Wea. Forecasting*, **9**, 301–315, [https://doi.org/10.1175/1520-0434\(1994\)009<0301:OTIOTI>2.0.CO;2](https://doi.org/10.1175/1520-0434(1994)009<0301:OTIOTI>2.0.CO;2).
- Blumberg, W. G., K. T. Halbert, T. A. Supinie, P. T. Marsh, R. L. Thompson, and J. A. Hart, 2017: SHARPPy: An open-source sounding analysis toolkit for the atmospheric sciences. *Bull. Amer. Meteor. Soc.*, **98**, 1625–1636, <https://doi.org/10.1175/BAMS-D-15-00309.1>.
- Boisier, J. P., R. Rondanelli, R. D. Garreaud, and F. Muñoz, 2016: Anthropogenic and natural contributions to the southeast Pacific precipitation decline and recent megadrought in central Chile. *Geophys. Res. Lett.*, **43**, 413–421, <https://doi.org/10.1002/2015GL067265>.
- Braun, S. A., and J. P. Monteverdi, 1991: An analysis of a mesocyclone-induced tornado occurrence in Northern California. *Wea. Forecasting*, **6**, 13–31, [https://doi.org/10.1175/1520-0434\(1991\)006<0013:AAOAMT>2.0.CO;2](https://doi.org/10.1175/1520-0434(1991)006<0013:AAOAMT>2.0.CO;2).
- Brooks, H. E., 2009: Proximity soundings for severe convection for Europe and the United States from reanalysis data. *Atmos. Res.*, **93**, 546–553, <https://doi.org/10.1016/j.atmosres.2008.10.005>.
- , and C. A. Doswell, 2001: Normalized damage from major tornadoes in the United States. *Wea. Forecasting*, **16**, 168–176, [https://doi.org/10.1175/1520-0434\(2001\)016<0168:NDFMTI>2.0.CO;2](https://doi.org/10.1175/1520-0434(2001)016<0168:NDFMTI>2.0.CO;2).
- , J. W. Lee, and J. P. Craven, 2003: The spatial distribution of severe thunderstorm and tornado environments from global reanalysis data. *Atmos. Res.*, **67–68**, 73–94, [https://doi.org/10.1016/S0169-8095\(03\)00045-0](https://doi.org/10.1016/S0169-8095(03)00045-0).
- , and Coauthors, 2019: A century of progress in severe convective storm research and forecasting. *A Century of Progress in Atmospheric and Related Sciences: Celebrating the American Meteorological Society Centennial*, Meteor. Monogr., No. 59, Amer. Meteor. Soc., <https://doi.org/10.1175/AMSMONOGRAPHS-D-18-0026.1>.
- Brunner, J. C., S. A. Ackerman, A. S. Bachmeier, and R. M. Rabin, 2007: A quantitative analysis of the enhanced-V feature in relation to severe weather. *Wea. Forecasting*, **22**, 853–872, <https://doi.org/10.1175/WAF1022.1>.
- Bunkers, M. J., D. A. Barber, R. L. Thompson, R. Edwards, and J. Garner, 2014: Choosing a universal mean wind for supercell motion prediction. *J. Operat. Meteor.*, **2**, 115–129, <https://doi.org/10.15191/nwajom.2014.0211>.
- Childs, S. J., R. S. Schumacher, and J. T. Allen, 2018: Cold-season tornadoes: Climatological and meteorological insights. *Wea. Forecasting*, **33**, 671–691, <https://doi.org/10.1175/WAF-D-17-0120.1>.
- Clark, M. R., 2009: The southern England tornadoes of 30 December 2006: Case study of a tornadic storm in a low CAPE, high shear environment. *Atmos. Res.*, **93**, 50–65, <https://doi.org/10.1016/j.atmosres.2008.10.008>.
- Coffer, B. E., and M. D. Parker, 2017: Simulated supercells in nontornadic and tornadic VORTEX2 environments. *Mon. Wea. Rev.*, **145**, 149–180, <https://doi.org/10.1175/MWR-D-16-0226.1>.
- , M. D. Parker, R. L. Thompson, B. T. Smith, and R. E. Jewell, 2019: Using near-ground storm relative helicity in supercell tornado forecasting. *Wea. Forecasting*, **34**, 1417–1435, <https://doi.org/10.1175/WAF-D-19-0115.1>.
- Davies-Jones, R. P., 1990: Test of helicity as a forecast parameter. Preprints, *16th Conf. on Severe Local Storms*, Amer. Meteor. Soc., Kananaskis Park, AB, Canada, 588–592.
- de Ovalle, A., 1703: *An Historical Relation of the Kingdom of Chile*. A. and J. Churchill, 154 pp.
- Edwards, R., J. G. LaDue, J. T. Ferree, K. Scharfenberg, C. Maier, and W. L. Coulbourne, 2013: Tornado intensity estimation: Past, present, and future. *Bull. Amer. Meteor. Soc.*, **94**, 641–653, <https://doi.org/10.1175/BAMS-D-11-00006.1>.
- Esterheld, J. M., and D. J. Giuliano, 2008: Discriminating between tornadic and non-tornadic supercells: A new hodograph technique. *Electron. J. Severe Storms Meteor.*, **3** (2), <http://ejssm.org/ojs/index.php/ejssm/article/viewArticle/33>.
- EUMETSAT, 2009: Best practices for RGB compositing of multi-spectral imagery. User Services Division, 8 pp., [http://oiswww.eumetsat.int/~ids/html/doc/best\\_practices.pdf](http://oiswww.eumetsat.int/~ids/html/doc/best_practices.pdf).
- EUMETSAT, 2015: Airmass RGB. 17 pp., [http://oiswww.eumetsat.int/~ids/html/doc/airmass\\_interpretation.pdf](http://oiswww.eumetsat.int/~ids/html/doc/airmass_interpretation.pdf).
- Falvey, M., and R. Garreaud, 2007: Wintertime precipitation episodes in central Chile: Associated meteorological conditions and orographic influences. *J. Hydrometeorol.*, **8**, 171–193, <https://doi.org/10.1175/JHM562.1>.
- Fujita, T. T., 1982: Principle of stereoscopic height computations and their applications to stratospheric cirrus over severe thunderstorms. *J. Meteor. Soc. Japan*, **60**, 355–368, [https://doi.org/10.2151/jmsj1965.60.1\\_355](https://doi.org/10.2151/jmsj1965.60.1_355).
- Garreaud, R. D., M. Vuille, and A. C. Clement, 2003: The climate of the Altiplano: Observed current conditions and mechanisms of past changes. *Palaeogeogr. Palaeoclimatol. Palaeoecol.*, **194**, 5–22, [https://doi.org/10.1016/S0031-0182\(03\)00269-4](https://doi.org/10.1016/S0031-0182(03)00269-4).
- , M. G. Nicora, R. E. Bürgesser, and E. E. Ávila, 2014: Lightning in western Patagonia. *J. Geophys. Res. Atmos.*, **119**, 4471–4485, <https://doi.org/10.1002/2013JD021160>.
- Goliger, A. M., and R. V. Milford, 1998: A review of worldwide occurrence of tornadoes. *J. Wind Eng. Ind. Aerodyn.*, **74–76**, 111–121, [https://doi.org/10.1016/S0167-6105\(98\)00009-9](https://doi.org/10.1016/S0167-6105(98)00009-9).
- Guarriello, F., C. J. Nowotarski, and C. C. Epifanio, 2018: Effects of the low-level wind profile on outflow position and near-surface vertical vorticity in simulated supercell thunderstorms. *J. Atmos. Sci.*, **75**, 731–753, <https://doi.org/10.1175/JAS-D-17-0174.1>.
- Hales, J. E., 1985: Synoptic features associated with Los Angeles tornado occurrences. *Bull. Amer. Meteor. Soc.*, **66**, 657–662, <https://doi.org/10.1175/1520-0477-66.6.657>.
- Hanstrum, B. N., G. A. Mills, A. Watson, J. P. Monteverdi, and C. A. Doswell III, 2002: The cool-season tornadoes of California and southern Australia. *Wea. Forecasting*, **17**, 705–722, [https://doi.org/10.1175/1520-0434\(2002\)017<0705:TCSTOC>2.0.CO;2](https://doi.org/10.1175/1520-0434(2002)017<0705:TCSTOC>2.0.CO;2).
- Hersbach, H., and Coauthors, 2020: The ERA5 global reanalysis. *Quart. J. Roy. Meteor. Soc.*, **146**, 1999–2049, <https://doi.org/10.1002/qj.3803>.
- Houze, R. A., Jr., 2014. *Cloud Dynamics*. Academic Press, 496 pp.
- Hutchins, M. L., R. H. Holzworth, J. B. Brundell, and C. J. Rodger, 2012: Relative detection efficiency of the world wide lightning location network. *Radio Sci.*, **47**, RS6005, <https://doi.org/10.1029/2012RS005049>.
- Iacono, M. J., J. S. Delamere, E. J. Mlawer, M. W. Shephard, S. A. Clough, and W. D. Collins, 2008: Radiative forcing by long-lived greenhouse gases: Calculations with the AER radiative transfer models. *J. Geophys. Res.*, **113**, D13103, <https://doi.org/10.1029/2008JD009944>.
- Janjić, Z. I., 1994: The step-mountain eta coordinate model: Further developments of the convection, viscous sublayer, and turbulence closure schemes. *Mon. Wea. Rev.*, **122**, 927–945, [https://doi.org/10.1175/1520-0493\(1994\)122<0927:TSMECM>2.0.CO;2](https://doi.org/10.1175/1520-0493(1994)122<0927:TSMECM>2.0.CO;2).
- Kalthoff, N., and Coauthors, 2002: Mesoscale wind regimes in Chile at 30°S. *J. Appl. Meteor.*, **41**, 953–970, [https://doi.org/10.1175/1520-0450\(2002\)041<0953:MWRICA>2.0.CO;2](https://doi.org/10.1175/1520-0450(2002)041<0953:MWRICA>2.0.CO;2).
- Karstens, C. D., T. M. Samaras, B. D. Lee, W. A. Gallus Jr., and C. A. Finley, 2010: Near-ground pressure and wind measurements in tornadoes. *Mon. Wea. Rev.*, **138**, 2570–2588, <https://doi.org/10.1175/2010MWR3201.1>.
- Kato, R., and Coauthors, 2015: Analysis of the horizontal two-dimensional near-surface structure of a winter tornadic vortex using high-resolution in situ wind and pressure measurements. *J. Geophys. Res. Atmos.*, **120**, 5879–5894, <https://doi.org/10.1002/2014JD022878>.
- King, J. R., M. D. Parker, K. D. Sherburn, and G. M. Lackmann, 2017: Rapid evolution of cool season, low-CAPE severe thunderstorm environments. *Wea. Forecasting*, **32**, 763–779, <https://doi.org/10.1175/WAF-D-16-0141.1>.

- Kirk, P. J., 2014: An updated tornado climatology for the UK: 1981–2010. *Weather*, **69**, 171–175, <https://doi.org/10.1002/wea.2247>.
- Koronczay, D., and Coauthors, 2019: The source regions of whistlers. *J. Geophys. Res. Space Phys.*, **124**, 5082–5096, <https://doi.org/10.1029/2019JA026559>.
- Lemon, L. R., and C. A. Doswell, 1979: Severe thunderstorm evolution and mesocyclone structure as related to tornadogenesis. *Mon. Wea. Rev.*, **107**, 1184–1197, [https://doi.org/10.1175/1520-0493\(1979\)107<1184:STEAMS>2.0.CO;2](https://doi.org/10.1175/1520-0493(1979)107<1184:STEAMS>2.0.CO;2).
- Lensky, I. M., and D. Rosenfeld, 2008: Clouds–Aerosols–Precipitation Satellite Analysis Tool (CAPSAT). *Atmos. Chem. Phys.*, **8**, 6739–6753, <https://doi.org/10.5194/acp-8-6739-2008>.
- Marín, J. C., B. S. Barrett, and D. Pozo, 2020: The tornadoes of 30–31 May 2019 in south-central Chile: Sensitivity to topography and SST. *Atmos. Res.*, **249**, 105301, <https://doi.org/10.1016/j.atmosres.2020.105301>.
- Markowski, P., and Y. Richardson, 2011: *Mesoscale Meteorology in Midlatitudes*. John Wiley & Sons, 430 pp.
- Moller, A. R., C. A. Doswell, M. P. Foster, and G. R. Woodall, 1994: The operational recognition of supercell thunderstorm environments and storm structures. *Wea. Forecasting*, **9**, 327–347, [https://doi.org/10.1175/1520-0434\(1994\)009<0327:TOROST>2.0.CO;2](https://doi.org/10.1175/1520-0434(1994)009<0327:TOROST>2.0.CO;2).
- Monteriverdi, J. P., and J. Quadros, 1994: Convective and rotational parameters associated with three tornado episodes in northern and central California. *Wea. Forecasting*, **9**, 285–300, [https://doi.org/10.1175/1520-0434\(1994\)009<0285:CARPAW>2.0.CO;2](https://doi.org/10.1175/1520-0434(1994)009<0285:CARPAW>2.0.CO;2).
- , C. A. Doswell, and G. S. Lipari, 2003: Shear parameter thresholds for forecasting tornadic thunderstorms in northern and central California. *Wea. Forecasting*, **18**, 357–370, [https://doi.org/10.1175/1520-0434\(2003\)018<0357:SPTFFT>2.0.CO;2](https://doi.org/10.1175/1520-0434(2003)018<0357:SPTFFT>2.0.CO;2).
- Nakanishi, M., and H. Niino, 2004: An improved Mellor–Yamada level-3 model with condensation physics: Its design and verification. *Bound.-Layer Meteor.*, **112**, 1–31, <https://doi.org/10.1023/B:BOUN.0000020164.04146.98>.
- , and ———, 2006: An improved Mellor–Yamada level-3 model: Its numerical stability and application to a regional prediction of advection fog. *Bound.-Layer Meteor.*, **119**, 397–407, <https://doi.org/10.1007/s10546-005-9030-8>.
- Niu, G.-Y., and Coauthors, 2011: The community Noah land surface model with Multiparameterization options (Noah-MP): 1. Model description and evaluation with local-scale measurements. *J. Geophys. Res.*, **116**, D12109, <https://doi.org/10.1029/2010JD015139>.
- Painting, D. J., 2003: AMDAR reference manual. World Meteorological Organization Tech. Rep. WMO-958, 84 pp., [https://library.wmo.int/doc\\_num.php?explnum\\_id=9026](https://library.wmo.int/doc_num.php?explnum_id=9026).
- Pessi, A. T., and S. Businger, 2009: The impact of lightning data assimilation on a winter storm simulation over the North Pacific ocean. *Mon. Wea. Rev.*, **137**, 3177–3195, <https://doi.org/10.1175/2009MWR2765.1>.
- Peyraud, L., 2013: Analysis of the 18 July 2005 tornadic supercell over the Lake Geneva region. *Wea. Forecasting*, **28**, 1524–1551, <https://doi.org/10.1175/WAF-D-13-00022.1>.
- Rasmussen, E. A., and J. Turner, 2003: *Polar Lows: Mesoscale Weather Systems in the Polar Regions*. Cambridge University Press, 612 pp.
- Rasmussen, E. N., 2003: Refined supercell and tornado forecast parameters. *Wea. Forecasting*, **18**, 530–535, [https://doi.org/10.1175/1520-0434\(2003\)18<530:RSATFP>2.0.CO;2](https://doi.org/10.1175/1520-0434(2003)18<530:RSATFP>2.0.CO;2).
- , and D. O. Blanchard, 1998: A baseline climatology of sounding-derived supercell and tornado forecast parameters. *Wea. Forecasting*, **13**, 1148–1164, [https://doi.org/10.1175/1520-0434\(1998\)013<1148:ABCOSD>2.0.CO;2](https://doi.org/10.1175/1520-0434(1998)013<1148:ABCOSD>2.0.CO;2).
- Reed, R. J., and W. Blier, 1986: A further study of comma cloud development in the eastern Pacific. *Mon. Wea. Rev.*, **114**, 1696–1708, [https://doi.org/10.1175/1520-0493\(1986\)114<1696:AFSOCC>2.0.CO;2](https://doi.org/10.1175/1520-0493(1986)114<1696:AFSOCC>2.0.CO;2).
- Rose, S. F., P. V. Hobbs, J. D. Locatelli, and M. T. Stoelinga, 2004: A 10-yr climatology relating the locations of reported tornadoes to the quadrants of upper-level jet streaks. *Wea. Forecasting*, **19**, 301–309, [https://doi.org/10.1175/1520-0434\(2004\)019<0301:AYCRTL>2.0.CO;2](https://doi.org/10.1175/1520-0434(2004)019<0301:AYCRTL>2.0.CO;2).
- Servicio Meteorológico de la Armada de Chile, 2010: Evidencias de fenómenos del tipo Tornado en las costas de la VIII Región Del Biobío Y el Sur de Chile. Servicio Meteorológico de la Armada de Chile, [http://meteoarmada.directemar.cl/prontus\\_meteo/site/artic/20101214/pags/20101214135557.html](http://meteoarmada.directemar.cl/prontus_meteo/site/artic/20101214/pags/20101214135557.html).
- Sherburn, K. D., and M. D. Parker, 2019: The development of severe vortices within simulated high-shear, low-CAPE convection. *Mon. Wea. Rev.*, **147**, 2189–2216, <https://doi.org/10.1175/MWR-D-18-0246.1>.
- , ———, J. R. King, and G. M. Lackmann, 2016: Composite environments of severe and nonsevere high-shear, low-CAPE convective events. *Wea. Forecasting*, **31**, 1899–1927, <https://doi.org/10.1175/WAF-D-16-0086.1>.
- Silva Dias, M. A. F., 2011: An increase in the number of tornado reports in Brazil. *Wea. Climate Soc.*, **3**, 209–217, <https://doi.org/10.1175/2011WCAS1095.1>.
- Skamarock, W. C., and Coauthors, 2019: A description of the Advanced Research WRF Model version 4. NCAR Tech. Note NCAR/TN-556+STR, 162 pp., <https://doi.org/10.5065/1DFH-6P97>.
- Soliño, A., and M. A. Schwarzkopf, 1982: Ocurrencia de Tornados Sobre El Sector Sur Del Continente Americano. *Segundo Congreso Brasileiro de Meteorologia*, Anais, Pelotas.
- Taszarek, M., H. E. Brooks, B. Czernecki, P. Szuster, and K. Fortuniak, 2018: Climatological aspects of convective parameters over Europe: A comparison of ERA-interim and sounding data. *J. Climate*, **31**, 4281–4308, <https://doi.org/10.1175/JCLI-D-17-0596.1>.
- Thompson, G., P. R. Field, R. M. Rasmussen, and W. D. Hall, 2008: Explicit forecasts of winter precipitation using an improved bulk microphysics scheme. Part II: Implementation of a new snow parameterization. *Mon. Wea. Rev.*, **136**, 5095–5115, <https://doi.org/10.1175/2008MWR2387.1>.
- Thompson, R. L., C. M. Mead, and R. Edwards, 2007: Effective storm-relative helicity and bulk shear in supercell thunderstorm environments. *Wea. Forecasting*, **22**, 102–115, <https://doi.org/10.1175/WAF969.1>.
- Tsonevsky, I., C. A. Doswell, and H. E. Brooks, 2018: Early warnings of severe convection using the ECMWF extreme forecast index. *Wea. Forecasting*, **33**, 857–871, <https://doi.org/10.1175/WAF-D-18-0030.1>.
- Turman, B. N., and R. J. Tettelbach, 1980: Synoptic-scale satellite lightning observations in conjunction with tornadoes. *Mon. Wea. Rev.*, **108**, 1878–1882, [https://doi.org/10.1175/1520-0493\(1980\)108<1878:SSSLOI>2.0.CO;2](https://doi.org/10.1175/1520-0493(1980)108<1878:SSSLOI>2.0.CO;2).
- Vicencio, J., A. Reyes, S. Sánchez, R. Padilla, J. Crespo, and D. Campos, 2019: Informe Especial: Tornados en la Región del Biobío. Dirección Meteorológica de Chile, 39 pp., [http://archivos.meteochile.gob.cl/portaldmc/meteochile/documentos/DMC-InfoEspecial\\_TornadosBiobio\\_v5black.pdf](http://archivos.meteochile.gob.cl/portaldmc/meteochile/documentos/DMC-InfoEspecial_TornadosBiobio_v5black.pdf).
- Virts, K. S., J. M. Wallace, M. L. Hutchins, and R. H. Holzworth, 2013: Highlights of a new ground-based, hourly global lightning climatology. *Bull. Amer. Meteor. Soc.*, **94**, 1381–1391, <https://doi.org/10.1175/BAMS-D-12-00082.1>.
- Wesolek, E., and P. Mahieu, 2011: The F4 tornado of August 3, 2008, in northern France: Case study of a tornadic storm in a low CAPE environment. *Atmos. Res.*, **100**, 649–656, <https://doi.org/10.1016/j.atmosres.2010.09.003>.
- Wood, V. T., and L. W. White, 2011: A new parametric model of vortex tangential-wind profiles: Development, testing, and verification. *J. Atmos. Sci.*, **68**, 990–1006, <https://doi.org/10.1175/2011JAS3588.1>.
- Zipser, E. J., D. J. Cecil, C. Liu, S. W. Nesbitt, and D. P. Yorty, 2006: Where are the most intense thunderstorms on Earth? *Bull. Amer. Meteor. Soc.*, **87**, 1057–1072, <https://doi.org/10.1175/BAMS-87-8-1057>.